

AD_____

Award Number: W81XWH-04-1-0461

TITLE: Time-Resolved and Spectroscopic Three-Dimensional Optical Breast Tomography

PRINCIPAL INVESTIGATOR: Robert R. Alfano, Ph.D.

CONTRACTING ORGANIZATION: State University of New York
New York, NY 10019-2925

REPORT DATE: April 2007

TYPE OF REPORT: Annual

PREPARED FOR: U.S. Army Medical Research and Materiel Command
Fort Detrick, Maryland 21702-5012

DISTRIBUTION STATEMENT: Approved for Public Release;
Distribution Unlimited

The views, opinions and/or findings contained in this report are those of the author(s) and should not be construed as an official Department of the Army position, policy or decision unless so designated by other documentation.

REPORT DOCUMENTATION PAGE				Form Approved OMB No. 0704-0188	
Public reporting burden for this collection of information is estimated to average 1 hour per response, including the time for reviewing instructions, searching existing data sources, gathering and maintaining the data needed, and completing and reviewing this collection of information. Send comments regarding this burden estimate or any other aspect of this collection of information, including suggestions for reducing this burden to Department of Defense, Washington Headquarters Services, Directorate for Information Operations and Reports (0704-0188), 1215 Jefferson Davis Highway, Suite 1204, Arlington, VA 22202-4302. Respondents should be aware that notwithstanding any other provision of law, no person shall be subject to any penalty for failing to comply with a collection of information if it does not display a currently valid OMB control number. PLEASE DO NOT RETURN YOUR FORM TO THE ABOVE ADDRESS.					
1. REPORT DATE (DD-MM-YYYY) 01-04-2007		2. REPORT TYPE Annual		3. DATES COVERED (From - To) 1 Apr 2006 – 31 Mar 2007	
4. TITLE AND SUBTITLE Time-Resolved and Spectroscopic Three-Dimensional Optical Breast Tomography				5a. CONTRACT NUMBER	
				5b. GRANT NUMBER W81XWH-04-1-0461	
				5c. PROGRAM ELEMENT NUMBER	
6. AUTHOR(S) Robert R. Alfano, Ph.D. E-Mail: alfano@sci.ccny.cuny.edu				5d. PROJECT NUMBER	
				5e. TASK NUMBER	
				5f. WORK UNIT NUMBER	
7. PERFORMING ORGANIZATION NAME(S) AND ADDRESS(ES) State University of New York New York, NY 10019-2925				8. PERFORMING ORGANIZATION REPORT NUMBER	
9. SPONSORING / MONITORING AGENCY NAME(S) AND ADDRESS(ES) U.S. Army Medical Research and Materiel Command Fort Detrick, Maryland 21702-5012				10. SPONSOR/MONITOR'S ACRONYM(S)	
				11. SPONSOR/MONITOR'S REPORT NUMBER(S)	
12. DISTRIBUTION / AVAILABILITY STATEMENT Approved for Public Release; Distribution Unlimited					
13. SUPPLEMENTARY NOTES – Original contains colored plates: ALL DTIC reproductions will be in black and white.					
14. ABSTRACT <p>The research carried out during the current reporting period included: (a) Use of optical tomographic imaging using independent component analysis (OPTICA) developed during the first reporting period to image targets in ex vivo breast tissue specimens, (b) Extension of OPTICA for obtaining cross sectional image of targets in turbid media, (c) (d) Development of a forward model for scattered light intensity distribution in the backscattering geometry; and (e) Development of an approach for determination of light absorption, scattering characteristics and anisotropy factor of a highly scattering medium using backscattered circular polarized light.</p> <p>The OPTICA approach was able to detect and provide the location of a tumor in a model breast composed of ex vivo breast tissues, and of a fluorescent target inside another model breast with millimeter accuracy. The forward model is suitable for describing polarized light propagation and imaging in backscattering geometry. Oblique incidence backscattering method for determination of optical properties has potential application in identifying breast tissue specimen as normal or cancerous. These developments prepare us for undertaking in vivo measurements.</p> <p>The graduate student supported by the project defended his Ph. D. thesis, adding another scientist to the ongoing fight against breast cancer.</p>					
15. SUBJECT TERMS breast cancer, near-infrared imaging, fluorescence imaging, tomography, target localization, optical tomography using independent component analysis (OPTICA)					
16. SECURITY CLASSIFICATION OF:			17. LIMITATION OF ABSTRACT	18. NUMBER OF PAGES	19a. NAME OF RESPONSIBLE PERSON
a. REPORT	b. ABSTRACT	c. THIS PAGE			USAMRMC
U	U	U	UU	36	19b. TELEPHONE NUMBER (include area code)

Table of Contents

	Page
Introduction.....	4
Body.....	4
Key Research Accomplishments.....	7
Reportable Outcomes.....	8
Conclusions.....	8
References.....	10
Appendices.....	11

4. INTRODUCTION

The goal of the research project, “Time-Resolved and Spectroscopic Three-Dimensional Optical Breast Tomography,” is to develop a safe and affordable breast cancer detection modality that uses noninvasive near-infrared (NIR) light for imaging, locating and diagnosing tumors in human breast with high resolution and specificity. The research focuses on the development and application of: (a) continuous wave (CW) and time-resolved experimental approaches for probing the target using NIR light, and (b) image reconstruction and target localization algorithms for obtaining target location and generating three-dimensional (3-D) tomographic images.

Significant progress has been made in both the thrust areas during the reporting period (May 1, 2006 – April 30, 2007) covered by this report.

5. BODY

The tasks performed and the progresses made during the current reporting period are as follows:

- Use of optical tomographic imaging using independent component analysis (OPTICA) developed during the first reporting period to image targets in *ex vivo* breast tissue specimens,
- Extension of OPTICA for obtaining cross sectional image of targets in turbid media,
- Development of a forward model for scattered light intensity distribution in the backscattering geometry; and
- Development of an approach for determination of light absorption and scattering characteristics and anisotropy factor of a highly scattering medium using backscattered circular polarized light.

We provide a brief outline of our accomplishments in these areas, and refer to appended publications for detailed description where applicable.

5.1. Imaging and localization of fluorescent targets embedded in *ex vivo* breast tissue specimen

We used the experimental arrangements^{1,2} that were set up and tested [Technical Objective (TO) 1, Task 1] during the first reporting period and detailed in the first report³ to carry out imaging and localization measurements on realistic breast models assembled using *ex vivo* breast tissues (TO 1, Task 2 and TO 2, Task 4). Fluorescent contrast agents and native fluorescence have the potential to enhance contrast of tumors compared to the normal tissue. So, one of our aims was to explore the feasibility of imaging and locating a fluorescent target inside the model breast.

The *ex vivo* female breast tissue specimen was a 100 mm X 100 mm X 26 mm slab held inside a transparent plastic box. The fluorescent target was a glass sphere (outer diameter ~4 mm and inner diameter 3.2 mm) filled with a solution of indocyanine green (ICG) dye in water. The water solution of ICG had an absorption coefficient of 11.5 cm^{-1} at 784 nm, and fluoresced over the 790-966 nm spectral range with a peak at 825 nm.

A 200- μm optical fiber delivered a 784-nm, 300 mW continuous-wave beam from a diode laser for sample illumination. The beam was collimated to a 1-mm spot onto the entrance face (the ‘source plane’) of the slab sample. Multiple source illumination was realized in practice by step scanning the slab samples across the laser beam in an 18 X 15 x - y array of grid points with a step size of 2.5 mm using a computer controlled translation stage. The signal from the opposite face of the sample (the ‘detection plane’) was passed through a narrow-band interference filter centered at 830 nm (FWHM \sim 10 nm, 50% transmission) to block the scattered 784-nm pump light. A camera lens collected the fraction of filtered fluorescence around 830 nm and projected it onto the sensing element of a cooled 16-bit, 1024 x 1024-pixel charged couple device (CCD) camera. Each illuminated pixel of the CCD camera could be regarded as a detector.

Each raw image was then cropped to select out the information-rich region, and binned to enhance the signal-to-noise ratio. All the binned images corresponding to illumination of the grid points in sequence were then stacked, and used as input for independent component analysis. The details of the analysis method, theoretical formalism, target localization algorithm, and experimental arrangement have been published,⁴ and are presented in *Appendix 1: “Three-dimensional localization and cross section reconstruction of fluorescent targets in ex vivo breast tissue using independent component analysis,” Appl. Phys. Lett. 89, 133902 (2006).*

The key result is that the x - y - z location of the target was determined to be (30 mm, 27 mm, 15 mm), while the known position was (30 mm, 27 mm, 16 mm). The lateral position of the target was determined exactly, while the axial position was determined to within 1 mm, which is quite remarkable!

5.2. Extension of OPTICA for obtaining cross sectional image of targets in turbid media

Another important development during the current reporting period has been the extension of OPTICA to estimate the size and shape of the target (such as, tumor) inside the turbid medium (such as, breast). OPTICA was initially developed^{1,2} to obtain accurate three-dimensional position information. The extension of the formalism to generate size and shape information provides inverse image reconstruction ability (*TO 3*) and its application to targets inside realistic human breast models (*TO4, Task 9*) is a crucial step towards *in vivo* breast imaging.

In this extension of OPTICA, the size and shape of the j -th target within the sample is estimated from a back-projection of the signal due to the target from the detection plane onto the target plane. Independent component analysis (ICA) provides an estimate of the contribution $U_{mj}(\mathbf{r}_d, \mathbf{r}_j, \omega)$ of the j -th target to the overall signal $U_m(\mathbf{r}_d, \mathbf{r}_j, \omega)$ due to all the targets, where \mathbf{r}_d and \mathbf{r}_j are the positions of the detector plane and the j -th target respectively. The mathematical formalism for obtaining the cross sectional image is summarized in Eq. (4) and Eq. (5) of Reference 1 (*Appendix 1*), which also provides examples of the application of the formalism to realistic breast model (*TO 4, Task 9*).

The efficacy of the extended OPTICA formalism was tested in the experiment involving *ex vivo* human breast tissue described in Section 5.1 above. The full width at half maximum height (FWHM) of the fluorescent sphere was determined to be 4 mm along x and y coordinate axes which agree with the known diameter of the fluorescent sphere target.

5.3. Localization and cross section imaging of a tumor in a model breast sample

The OPTICA formalism along with its extension for obtaining cross section images was then applied to a model human breast sample assembled using *ex vivo* breast tissues (*TO1, Task 2; TO 4, Task 9*). In this application the difference in light scattering characteristics of the tumor and different breast tissue components was used for target detection. The details of the experimental arrangement, theoretical formalism, and results are presented in *Appendix 2: “Optical high resolution cross section imaging of a human breast model using independent component analysis in CW and time domain,” Proceedings of SPIE, Vol.6434, 643416 (2007)*.

The sample breast had a dimension of 42 mm X 33 mm X 30 mm. A tumor of dimension 5 mm X 5 mm X 3 mm was placed at the mid-plane of the breast sample. The sample was illuminated in by CW 784 nm beam from a diode laser delivered by a 200- μ m optical fiber. Multiple source illumination was realized by step scanning the sample in 2-mm steps over an array of 22 X 16 grid points along the horizontal (x) and vertical (y) directions across the laser beam. After optical measurements, the sample was transferred to our collaborators at the New York Eye and Ear Infirmary for pathological study and correlation (*TO2, Task 5*).

The key results are as follows. (a) The location of the tumor was determined to within 1 mm in all three dimensions (details in Fig. 2, *Appendix 2*); (b) the FWHM of the tumor is estimated to be ~ 11 mm (details in Fig. 3, *Appendix 2*); (c) Two other structures with weaker scattering coefficients were identified in the mid-plane of the sample. Since normal component of the breast tissue specimen was mainly adipose tissue, we tentatively identified these two components as the fibro-glandular tissues. Comparison with the pathology results further confirmed the identity of the tumor and the fibro-glandular tissues.

5.4. Development of a forward model for scattered light intensity distribution in the backscattering geometry

While the approaches highlighted above use experimental data in transillumination geometry, an approach based on backscattering geometry will be advantageous for targets closer to the input plane, and for obtaining depth location. We developed an analytical cumulant solution of both the time-dependent scalar radiative transfer equation (SRTE), and the vector radiative transfer equation (VRTE) in an infinite uniform medium.^{5,6} The solution of SRTE is suitable for describing scattered photon density distribution for an arbitrary phase function as long as it is a function of the scattering angle. The numerical results of light propagation from the analytical solution are in a good agreement with that of Monte Carlo simulation.⁷

However, the SRTE cannot account for the polarization of the incident and scattered light beams. Polarization is an important parameter and its evolution as a polarized beam of light interacts with a scattering medium with embedded targets can provide useful imaging information. To capitalize on the advantages that polarization has to offer, we used the analytical solution of the VRTE to study the backscattering of circularly polarized light pulses from an infinite uniform scattering medium as a function of the helicity of the incident light and size of scatterers in the medium (*TO3, Task 6*). The formalism considers a polarized short pulse of light incident on the scattering medium, uses the analytical cumulant solution of the VRTE with the phase matrix obtained from the Mie theory to calculate the temporal profile of scattered polarized photons for any position and any angle of detection. The details of the formalism, results, and comparison with experimental results are presented in *Appendix 3: “Analytical*

cumulant solution of the vector radiative transfer equation investigates backscattering of circularly polarized light from turbid media,” Phys. Rev. E **74**, 056605 (2006).

The results show that circularly polarized light of the same helicity dominates the backscattered signal when scatterer size is larger than the wavelength of light. For the smaller particle size, light of opposite helicity makes the dominant contribution to the backscattered signal, as shown in Figure 1 in *Appendix 3*. The conclusion is in good agreement with experimental results, as displayed in Fig. 6 of *Appendix 3*. The characteristic change of circular polarization of backscattering light with size of scatterers may provide a new method to directly determine microscopic size of scatterers which is useful for highlighting tumors from normal tissues.

5.5. Determination of light absorption, scattering characteristics and anisotropy factor

We are developing a technique to determine scattering coefficient (μ_s), absorption coefficient (μ_a), and anisotropy factor (g) of breast tissue specimens using backscattering of light of different wavelengths (*TO 2, Task 4*). The approach involves illumination of the surface of the specimen with circularly polarized light at an oblique angle of incidence ($\sim 70^\circ$) and measurement of the backscattered co-polarized and cross-polarized light. From the backscattered diffuse reflectance data the absorption coefficient (μ_a), and the reduced scattering coefficient (μ_s') are determined at different wavelengths. The wavelength dependence of the reduced scattering coefficient, μ_s' is used to extract the fractal dimension (D_f) of the specimen. The depolarized diffuse reflection data and these three parameters are then used to extract the anisotropy factor (g). The g -factor provides a useful probe of the size of the scatterers and serves as a fingerprint for discriminating between normal and cancerous tissues. The approach may prove useful in lumpectomy, where the surgeon looks for the margins of the tumor with high accuracy.

Details of the experimental method and approach to extract key parameters are presented in *Appendix 4*: “Determination of light absorption, scattering and anisotropy factor of a highly scattering medium using backscattered circular polarized light,” *Proceedings of SPIE* Vol. 6435, 64350J (2007).

6. KEY RESEARCH ACCOMPLISHMENTS

- Demonstrated the efficacy of Optical Tomography using Independent Component Analysis (OPTICA) approach for detection, 3-D localization, and cross section imaging of a fluorescent target in breast tissue specimens and model medium. (*Appendix 1*).
- The location of a tumor inside a realistic breast model composed of excised breast tissues was determined with millimeter accuracy (*Appendix 2*).
- Developed a forward model for determining the backscattered polarized light intensity distribution (*Appendix 3*).
- Developing a technique to determine scattering coefficient (μ_s), absorption coefficient (μ_a), and anisotropy factor (g) of breast tissue specimens that has potential application in optical biopsy, that is, for determining if the tissue specimen is normal or cancerous (*Appendix 4*).

7. REPORTABLE OUTCOMES

Ph. D. Thesis

M. Alrubaiee, the graduate student whose research was supported in part by this grant, successfully defended his Ph. D. thesis entitled, “*Time-resolved and Continuous Wave Spectroscopic Imaging of Biological Media.*”

Journal Articles

1. M. Alrubaiee, M. Xu, S. K. Gayen, and R. R. Alfano, “Three-dimensional localization and cross section reconstruction of fluorescent targets in *ex vivo* breast tissue using independent component analysis,” *Appl. Phys. Lett.* **89**, 133902 (2006).
2. W. Cai, Xiaohui Ni, S. K. Gayen, and R. R. Alfano, “Analytical cumulant solution of the vector radiative transfer equation investigates backscattering of circularly polarized light from turbid media,” *Phys. Rev. E* **74**, 056605 (2006).

Conference Proceedings

3. M. Xu, M. Alrubaiee, S. K. Gayen, and R. R. Alfano, “Optical high resolution cross section imaging of a human breast model using independent component analysis in CW and time domain.” *Proceedings of SPIE*, Vol.6434, 643416 (2007).
4. M. Xu, M. Alrubaiee, S. K. Gayen, and R. R. Alfano, “Determination of light absorption, scattering and anisotropy factor of a highly scattering medium using backscattered circular polarized light.” *Proceedings of SPIE* Vol. 6435, 64350J (2007).

Presentations

1. M. Xu, M. Alrubaiee, S. K. Gayen, and R. R. Alfano, “Optical high resolution cross section imaging of a human breast model using independent component analysis in CW and time domain.” Paper 6934-42 presented at Conference 6934: Optical Tomography and Spectroscopy of Tissue VII of SPIE’s BiOS 2007/ Photonics West, January 20-25, 2007, San Jose, California.
2. M. Xu, M. Alrubaiee, S. K. Gayen, and R. R. Alfano, “Determination of light absorption, scattering and anisotropy factor of a highly scattering medium using backscattered circular polarized light.” Paper 6935-18 presented at Conference 6435: Optical Interactions with Tissue and Cells XVIII of SPIE’s BiOS 2007/ Photonics West, January 20-25, 2007, San Jose, California.
3. M. Xu, M. Alrubaiee, S. K. Gayen and R. R. Alfano, “Optical high resolution cross section imaging of human breast using independent component analysis.” Presented at the 5th *Inter-Institute Workshop on Optical Diagnostic Imaging from Bench to Bedside at the National Institutes of Health*, 25-27 September 2006, Bethesda, Maryland, USA.

8. CONCLUSION

The work carried out during this reporting period shows the potential for detection and three-dimensional localization of targets (including tumor) within a turbid medium (including model breasts formed with *ex vivo* tissues) with significant accuracy based on the differences in the

scattering, absorption, and fluorescence characteristics of the target (*e.g.*, tumor) and the intervening medium (*e.g.*, normal breast tissue).

“So What Section”

- The completion of the Ph. D thesis by the graduate student supported by the grant is important since it adds another scientist to the ongoing struggle against cancer.
- A recent study involving 35,319 patients underscores the influence of primary tumor location on breast cancer prognosis, and makes it imperative that breast cancer detection modalities obtain three dimensional (3-D) location of the tumor relative to the axilla.⁸ The current work is an important development in obtaining noninvasive 3-D location of a tumor within the breast.
- The applicability of OPTICA for scattering, absorptive, and fluorescent targets makes it versatile since all three phenomena may be used for contrast enhancement between the tumor and normal breast tissues. Fluorescence-based detection may require use of contrast agents, such as, molecular beacons.
- Three-dimensional target localization will enable closer probing of a smaller volume around of the target providing more details since smaller pixel size could be used without increasing the computation time (as a smaller volume will be probed).
- Further development of the OPTICA, and the development of the oblique angle backscattering have potential application in lumpectomy, where the surgeon looks for the margins of the tumor with high accuracy.
- What is more important, the work accomplished so far prepares us for the next step, *in vivo* optical breast imaging involving volunteers.

9. REFERENCES

1. M. Xu, M. Alrubaiee, S. K. Gayen and R. R. Alfano, "Three-dimensional optical imaging of objects in a turbid medium using independent component analysis: theory and simulation," *J. Biomed. Opt.* **10**, 051705 (2005).
2. M. Alrubaiee, M. Xu, S. K. Gayen, M. Brito, and R. R. Alfano, "Three-dimensional optical tomographic imaging of objects in tissue-simulating turbid medium using independent component analysis," *Appl. Phys. Lett.* **87**, 191112 (2005).
3. First technical report of this project covering the period 5/1/2004 – 4/30/2006
4. M. Alrubaiee, M. Xu, S. K. Gayen, and R. R. Alfano, "Three-dimensional localization and cross section reconstruction of fluorescent targets in *ex vivo* breast tissue using independent component analysis," *Appl. Phys. Lett.* **89**, 133902 (2006).
5. W. Cai, M. Lax, R. R. Alfano, "Analytical solution of the elastic Boltzmann transport equation in an infinite uniform medium using cumulant expansion" *J. Phys. Chem. B* **104** 3996-4000 (2000).
6. W. Cai, M. Lax, R. R. Alfano, "Analytical solution of the polarized photon transport equation in an infinite uniform medium using cumulant expansion" *Phys. Rev. E* **63**, 016606 (2001).
7. W. Cai, M. Xu, R. R. Alfano, "Analytical form of the particle distribution based on the cumulant solution of the elastic Boltzmann transport equation" *Phys. Rev. E* **71** 041202 (2005).
8. N. Kroman, J. Wohlfahrt, H. T. Mouridsen, and M. Melbye, "Influence of tumor location on breast cancer prognosis," *Int. J. Cancer* **105**, 542 -545 (2003).

10. APPENDICES

- Appendix 1.* M. Alrubaiee, M. Xu, S. K. Gayen, and R. R. Alfano, “Three-dimensional localization and cross section reconstruction of fluorescent targets in *ex vivo* breast tissue using independent component analysis,” *Appl. Phys. Lett.* **89**, 133902 (2006).
- Appendix 2.* M. Xu, M. Alrubaiee, S. K. Gayen, and R. R. Alfano, “Optical high resolution cross section imaging of a human breast model using independent component analysis in CW and time domain.” *Proceedings of SPIE*, Vol.6434, 643416 (2007).
- Appendix 3.* W. Cai, Xiaohui Ni, S. K. Gayen, and R. R. Alfano, “Analytical cumulant solution of the vector radiative transfer equation investigates backscattering of circularly polarized light from turbid media,” *Phys. Rev. E* **74**, 056605 (2006).
- Appendix 4.* M. Xu, M. Alrubaiee, S. K. Gayen, and R. R. Alfano, “Determination of light absorption, scattering and anisotropy factor of a highly scattering medium using backscattered circular polarized light.” *Proceedings of SPIE* Vol. 6435, 64350J (2007).

Localization and cross section reconstruction of fluorescent targets in *ex vivo* breast tissue using independent component analysis

M. Alrubaiee,^{a)} M. Xu, S. K. Gayen, and R. R. Alfano

Institute for Ultrafast Spectroscopy and Lasers, Physics Department, The City College of New York of the City University of New York, 138th Street, Convent Avenue, New York, New York 10031

(Received 21 February 2006; accepted 24 July 2006; published online 27 September 2006)

An information theory based approach is introduced for the detection and three-dimensional localization of fluorescent targets embedded in a turbid medium. The approach uses multisource illumination of the medium, multidetector transillumination acquisition of fluorescence signal, independent component analysis for target detection and localization, and a back-projection algorithm for reconstruction of target cross section. The efficacy of the approach is demonstrated by locating and estimating the cross section of a fluorescent target embedded in a $100 \times 100 \times 26 \text{ mm}^3$ *ex vivo* human breast tissue specimen and in a tissue-simulating turbid medium of thickness 50 times the transport mean free path. © 2006 American Institute of Physics. [DOI: 10.1063/1.2356024]

Development of optical fluorescence tomography is of interest for cancer detection and diagnosis.^{1–4} The recent advent of fluorescence beacons and contrast agents with the ability to attach themselves to desired abnormal cells or organelles⁵ enhances the target specificity and diagnostic potential of fluorescence based optical imaging approaches. Determination of accurate location of targets embedded in a turbid medium remains a formidable task for both direct imaging and inverse image reconstruction approaches and for all types of targets—fluorescent, absorptive, and scattering.^{6–11} We have introduced an approach, known as optical tomography using independent component analysis (OPTICA), that enables more accurate determination of target location in turbid media than existing optical methods.^{12,13} It uses multisource optical probing of the sample, multidetector acquisition of transmitted signal, and independent component analysis¹⁴ of information theory to analyze the signal for three-dimensional (3D) localization and characterization of the target. The efficacy of OPTICA for locating small absorptive and scattering targets embedded in turbid media has been demonstrated.^{11,15} In this letter, OPTICA formalism is extended for fluorescent targets, and its efficacy is tested by obtaining 3D location and cross sectional image of a fluorescent target in an *ex vivo* human breast tissue sample and in a tissue-simulating turbid medium from experimental data.

The theoretical formalism for fluorescence OPTICA is based on the premise that the spatial distribution of the light intensity at the exit boundary of the medium is a weighted mixture of signals arriving from the fluorescent targets (“sources”) embedded in the medium:

$$x(\mathbf{r}_d, \mathbf{r}_s) = \sum_j a_j(\mathbf{r}_d) s_j(\mathbf{r}_s), \quad (1)$$

where $a_j(\mathbf{r}_d)$ is the mixing vector and $a_j(\mathbf{r}_d) s_j(\mathbf{r}_s)$ represents the contribution of the j th target to the fluorescent signal at the detector plane for illumination of the source plane at \mathbf{r}_s . Independent component analysis assumes that these fluorescent sources are independent, treats the problem of detecting those as a source separation problem, and obtains a_j and s_j

by seeking maximal mutual independence between s_j 's.^{12,14}

Light propagation in a highly scattering medium with an embedded fluorescent target excited by an external light source is approximately described by coupled diffusion equations at the excitation and emission wavelengths.^{16,17} The fluorescence signal $U_m(\mathbf{r}_d, \mathbf{r}_s, \omega)$ can be expressed in terms of the two Green's functions $G_x(\mathbf{r}, \mathbf{r}_s, \omega)$ and $G_m(\mathbf{r}_d, \mathbf{r}, \omega)$ describing light propagation from the excitation source at \mathbf{r}_s to the fluorescent target at \mathbf{r} at the excitation wavelength λ_x and the light propagation from the target to the detector at \mathbf{r}_d at the emission wavelength λ_m . In this letter we report on slab samples. Consequently, Green's functions for a slab geometry¹⁸ under the diffusion approximation of the equation of radiative transfer are used.

Assuming that the j th fluorescent target is contained in volume V_j centered at \mathbf{r}_j , the fluorescence signal under excitation by a unit point source at \mathbf{r}_s is given by

$$U_m(\mathbf{r}_d, \mathbf{r}_s, \omega) = \sum_{j=1}^j G_m(\mathbf{r}_d, \mathbf{r}_j, \omega) f_j(\omega) G_x(\mathbf{r}_j, \mathbf{r}_s, \omega), \quad (2)$$

where $f_j(\omega) = \gamma(\mathbf{r}_j) c V_j / [1 - i\omega\tau(\mathbf{r}_j)]$ represents the fluorescence signal strength of the j th target, γ is the fluorescent yield, c is the speed of light in medium, τ is the fluorescence lifetime, and ω is the angular modulation frequency of the excitation light intensity.

Both the location and the strength of the j th target can be computed by using a least square fitting procedure:

$$\min_{\mathbf{r}_j, \alpha_j, \beta_j} \left\{ \sum_{\mathbf{r}_s} [\alpha_j^{-1} s_j(\mathbf{r}_s) - G_x(\mathbf{r}_j, \mathbf{r}_s, \omega)]^2 + \sum_{\mathbf{r}_d} [\beta_j^{-1} a_j(\mathbf{r}_d) - G_m(\mathbf{r}_d, \mathbf{r}_j, \omega)]^2 \right\}, \quad (3)$$

where $s_j(\mathbf{r}_s) \propto G_x(\mathbf{r}_j, \mathbf{r}_s, \omega)$ and $a_j(\mathbf{r}_d) \propto G_m(\mathbf{r}_d, \mathbf{r}_j, \omega)$. The fitting yields the location \mathbf{r}_j of and the two scaling constants α_j and β_j for the j th target. The fluorescence strength then is $f_j = \alpha_j \beta_j$.

The size and shape of the j th target can be estimated from a back projection of $U_m(\mathbf{r}_d, \mathbf{r}_s, \omega)$ from the detection plane onto the “target plane,” i.e., $z = z_j$ plane. The fluorescence signal from the j th target is approximated by

^{a)}Electronic mail: malrub@sci.cuny.cuny.edu

$$U_{m_j}(\mathbf{r}_d, \mathbf{r}_s, \omega) = \int G_m(\boldsymbol{\rho}_d - \boldsymbol{\rho}, \omega) X_j(\boldsymbol{\rho}) G_x(\boldsymbol{\rho} - \boldsymbol{\rho}_s, \omega) d\boldsymbol{\rho}, \quad (4)$$

where the integration is over the $z=z_j$ plane and $\boldsymbol{\rho}_d$ and $\boldsymbol{\rho}_s$ are the lateral coordinates of the detector and the source, respectively. In the Fourier space, $X_j(\mathbf{q})$ can be obtained from Eq. (4) as

$$X_j(\mathbf{q}) = \frac{U_{m_j}(\mathbf{q} - \mathbf{q}_s, \mathbf{q}_s, \omega)}{G_m(\mathbf{q} - \mathbf{q}_s, \omega) G_x^*(\mathbf{q}_s, \omega)}, \quad (5)$$

where \mathbf{q} and \mathbf{q}_s are the spatial frequencies on the x - y plane and $*$ denotes complex conjugate. The inverse Fourier transforms of $X_j(\mathbf{q})$ yield the cross sectional image of the fluorescent target in the $z=z_j$ plane. The full width at half maximum (FWHM) of the cross sectional image provides an estimate of the real target size. The cross sectional image is a two-dimensional (2D) distribution of the fluorescent object at the target plane.

The experimental arrangement to test the fluorescence OPTICA approach is shown schematically in Fig. 1(a). The fluorescent target was a glass sphere (outer diameter of ~ 4 mm and inner diameter of 3.2 mm) filled with a solution of indocyanine green (ICG) in water. The water solution of ICG had an absorption coefficient of 11.5 cm^{-1} at 784 nm and fluoresced over the 790–966 nm spectral range with a peak at 825 nm. The sphere was placed inside a $100 \times 100 \times 26 \text{ mm}^3$ slab of *ex vivo* female breast tissue specimen contained in a transparent plastic box. One of the sides of the box could be moved to uniformly compress and hold the tissue specimen in position. The breast tissue specimen consisted primarily of adipose tissue with small amount of skin and was provided to us by the National Disease Research Interchange under an Internal Review Board approval at the City College of New York. In another experiment to test if the approach could locate a target inside an average-size human female breast, the sphere was placed inside a $250 \times 250 \times 50 \text{ mm}^3$ transparent plastic cell filled with Intralipid-10% suspension in water. The concentration of Intralipid-10% was adjusted to provide transport lengths l_t of ~ 1 mm at 784 nm and 1.1 mm at 830 nm, which are within the reported range of values for healthy human breast tissues.¹⁹

A 200 μm optical fiber delivered a 784 nm, 300 mW continuous-wave beam from a diode laser for sample illumination. The beam was collimated to a 1 mm spot onto the entrance face (henceforth referred to as the “source plane”) of the slab samples. Multiple source illumination was realized in practice by step scanning the slab samples across the laser beam in an x - y array of grid points using a computer controlled translation stage. The x - y array was 18×15 for the tissue sample and 10×10 for the Intralipid-10% sample, with a step size of 2.5 mm for both the cases. The signal from the opposite face of the sample (henceforth referred to as the “detection plane”) was passed through a narrow-band interference filter centered at 830 nm (FWHM ~ 10 nm, 50% transmission) to block the scattered 784 nm pump light. A camera lens collected the fraction of filtered fluorescence around 830 nm and projected it onto the sensing element of a cooled 16 bit, 1024×1024 pixel charged couple device (CCD) camera. Each illuminated pixel of the CCD camera could be regarded as a detector. For illumination of every scanned point on the source plane, the CCD camera recorded

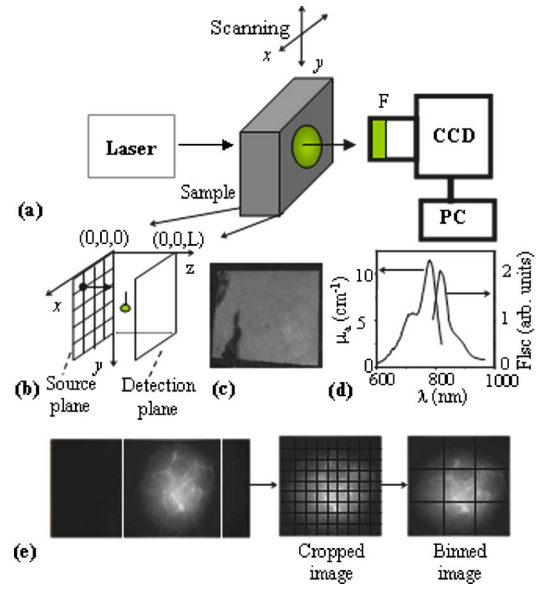


FIG. 1. (a) Schematic diagram of the experimental arrangement (CCD = charge coupled device camera, F = filter, PC = personal computer). (b) An expanded view of the sample input (source) plane and exit (detection) plane showing the grid points in the x - y plane. (c) A photograph of the exit face of the tissue sample. (d) Absorption and fluorescence spectra of the ICG dye solution in water. (e) A typical raw CCD image of the detection plane and how it is cropped and binned for analysis.

the diffusely transmitted 2D fluorescence intensity pattern on the detection plane. A second scan to estimate the average value of $\kappa = \sqrt{3\mu_a\mu_s'}$ (where μ_a and μ_s' are the absorption and scattering coefficients, respectively) of the background medium used a short-pass filter at 750 nm to block the fluores-

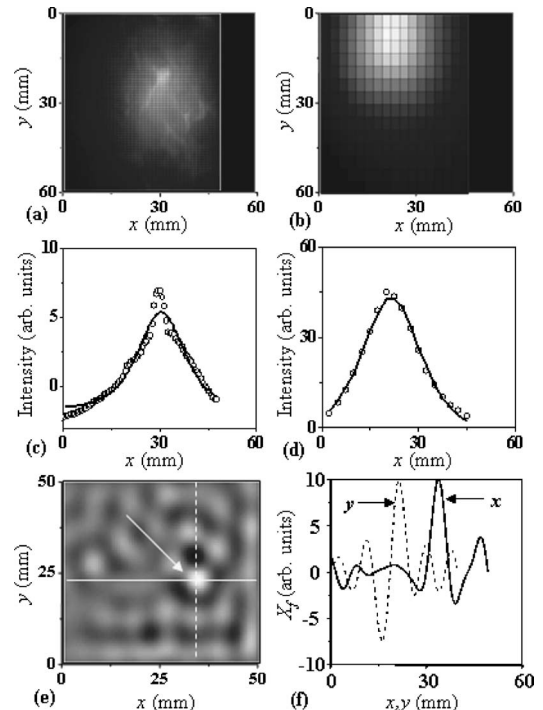


FIG. 2. OPTICA generated fluorescence intensity distribution on (a) the detector and (b) the source planes. [(c) and (d)] Green's function fits to the horizontal spatial profiles through the centers of intensity distributions in (a) and (b), respectively. (e) Cross sectional image at the $z=z_j$ plane. (f) Spatial profiles of the cross sectional image along the x and y directions shown by the white lines in (e).

TABLE I. Comparison of known positions and sizes of the target with OPTICA-determined values.

Samples	Known position (x, y, z) (mm)	Observed position (x, y, z) (mm)	Profile FWHM ^a ($\Delta x, \Delta y$) (mm)
Breast tissue <i>ex vivo</i>	(30, 27, 15)	(30, 27, 16)	(4, 4)
Intralipid-10% in water	(115, 115, 15)	(115, 115, 16)	(12, 12)

^aThe FWHM values should be compared with the inner diameter of 3.2 mm of the sphere.

cence signal and admit a very small fraction of the transmitted excitation light.

Figure 1(b) shows a photograph of the exit surface of the tissue sample. Figure 1(c) presents a typical 2D raw image (fluorescence intensity distribution) of the detection plane recorded by the CCD camera for illumination of a grid point in the source plane. Each raw image is then cropped to select out the information-rich region and binned to enhance the signal-to-noise ratio. All the binned images corresponding to illumination of the grid points in sequence are then stacked and used as input for independent component analysis.

Figures 2(a) and 2(b) present the OPTICA generated intensity distributions on the detector and source planes, respectively, of the tissue sample. The corresponding Green's function fits to horizontal profile through the center of intensity distributions are shown in Figs. 2(c) and 2(d), respectively. The (x, y, z) location of the target center obtained from this analysis is displayed in Table I. The lateral positions (x, y) agree completely, and the axial position agrees within 1 mm of the known values. The cross sectional image obtained using back-projection Fourier transforms in Eq. (5), is shown in Fig. 2(e). Figure 2(f) shows intensity profiles of the cross sectional image along the x and y directions shown by the white dotted lines in Fig. 2(e). The FWHM values of intensity profiles of the cross sectional image, presented in column 4 of Table I, are 4 mm, in good agreement with the known 3.2 mm inner diameter of the fluorescent sphere.

The results of measurements on the same fluorescent sphere embedded in Intralipid-10% suspension in water are also summarized in Table I. Again the lateral positions are in exact agreement, while the axial position agrees within 1 mm. However, the FWHM values of the intensity profiles of the cross sectional image are estimated to be 12 mm each, which is 3.7 times the 3.2 mm inner diameter of the sphere. We attribute this difference primarily to the much larger thickness ($50l_t$) of the Intralipid-10% sample than that of the tissue sample ($26l_t$). Spatial resolution decreases rapidly with sample thickness (for the same axial target position) because of the diffuse nature of light propagation through a highly scattering medium. Since the transport lengths (l_t) were comparable and the target was located 15 mm from the source plane for both the samples, the target-detector plane distance in Intralipid-10% sample was more than three times larger than that in the tissue sample, which in turn led to a much higher estimate for the target size. As the incident beam power was limited to 300 mW for both the samples, higher optical thickness resulted in much lower fluorescence signal-to-noise ratio for the Intralipid-10% sample, which in turn contributed to a higher estimate of the target cross section. Substantial improvements in target size estimate are expected if an intensified CCD camera for higher sensitivity, and more incident beam powers are used.

It should be noted that multisource measurements, though crucial for detection of multiple targets, might not be needed for a single target, since the position of the target determines the normalized fluorescence intensity distribution. However, multisource measurements help reduce the deleterious effects of noise and inaccuracy in the estimation of optical properties of the medium and provide better assessment of 3D location even in the case of a single target.

The simpler but important case involving a single target (e.g., a tumor in the breast) was chosen for experimental demonstration. In simulation the approach could locate three targets with one target $\sim 20l_t$ behind another in a $\sim 50l_t$ thick turbid medium. Localization of even more targets is possible and will be presented along with experimental results in a future publication.

In summary, OPTICA can provide rather accurate 3D location of a fluorescent target in a turbid medium and an estimate of its cross section.

This work is supported in part by PSC-CUNY, U.S. Army Medical Research and Materials Command (Grant No. W81XWH-04-1-0461), and NASA COSI program. The authors acknowledge Merlin Brito, David Matten, and Imtiaz Tanveer for technical support.

- ¹C. D'Andrea, L. Spinelli, D. Cornelli, G. Valentini, and R. Cubeddu, *Phys. Med. Biol.* **50**, 2313 (2005).
- ²I. Gannot, V. Chernomordik, A. Garashi, and A. Gandjbakhche, *Opt. Lett.* **29**, 742 (2004), and Ref. 7 therein.
- ³A. Eidsath, V. Chernomordik, A. Gandjbakhche, P. Smith, and A. Russo, *Phys. Med. Biol.* **47**, 4079 (2002), and Refs. 2, 5, and 6 therein.
- ⁴A. B. Thompson, D. J. Hawrysz, and E. M. Sevick-Muraca, *Appl. Opt.* **42**, 4125 (2003), and Ref. 8 therein.
- ⁵Sanjay Tyagi, Salvatore A. E. Marras, and Fred Russell Kramer, *Nat. Biotechnol.* **18**, 1191 (2000).
- ⁶Alexander D. Klose and Andreas H. Hielscher, *Opt. Lett.* **28**, 1019 (2003).
- ⁷M. A. O'Leary, D. A. Boas, X. D. Li, B. Chance, and A. G. Yodh, *Opt. Lett.* **21**, 158 (1996).
- ⁸W. Cai, S. K. Gayen, M. Xu, M. Zevallos, M. Alrubaiee, M. Lax, and R. R. Alfano, *Appl. Opt.* **38**, 4237 (1999).
- ⁹V. Ntziachristos and R. Weissleder, *Opt. Lett.* **26**, 893 (2001).
- ¹⁰S. R. Arridge, *Inverse Probl.* **15**, R41 (1999).
- ¹¹A. D. Kim and A. Ishimaru, *Appl. Opt.* **37**, 5313 (1998).
- ¹²M. Xu, M. Alrubaiee, S. K. Gayen, and R. R. Alfano, *Appl. Opt.* **44**, 1889 (2005).
- ¹³M. Xu, M. Alrubaiee, S. K. Gayen, and R. R. Alfano, *J. Biomed. Opt.* **44**, 1889 (2005).
- ¹⁴J.-F. Cardoso, *Proc. IEEE* **86**, 2009 (1998).
- ¹⁵M. Alrubaiee, M. Xu, S. K. Gayen, M. Brito, and R. R. Alfano, *Appl. Phys. Lett.* **87**, 191112 (2005).
- ¹⁶M. S. Patterson and B. W. Pogue, *Appl. Opt.* **33**, 1963 (1994).
- ¹⁷A. B. Milstein, S. Oh, K. J. Webb, C. A. Bouman, Q. Zhang, D. A. Boas, and R. P. Millane, *Appl. Opt.* **42**, 3081 (2003).
- ¹⁸M. Lax, V. Narayanamurti, and R. C. Fulton, in *Laser Optics of Condensed Matter*, edited by J. L. Birman, H. Z. Cummins, and A. A. Kaplyanskii (Plenum, New York, 1987), pp. 229–237.
- ¹⁹H. Heusmann, J. Kölzer, and G. Mitic, *J. Biomed. Opt.* **1**, 425 (1996).

Optical high resolution cross section imaging of a human breast model using independent component analysis

M. Xu^a, M. Alrubaiee^b, S. K. Gayen^b, H. Savage^c, and R. R. Alfano^b

^aDepartment of Physics, Fairfield University, Connecticut, CT 06824

^bInstitute for Ultrafast Spectroscopy and Lasers and Department of Physics,
The City College and Graduate Center of City University of New York, New York, NY 10031

^cDepartment of Otolaryngology, New York Eye and Ear Infirmary, New York, NY 10003
Email: mxu@mail.fairfield.edu

ABSTRACT

Optical imaging using independent component analysis (OPTICA) is enhanced to provide a high resolution cross section imaging of objects in a turbid medium by a backprojection technique. The performance is demonstrated by imaging a human breast model made of *ex vivo* human breast tissues. Cancerous site of 5mm size is detected at the midplane of the 33mm thick breast model. The reconstructed cross section image compares favorably with pathology findings.

Keywords: optical imaging, independent component analysis, cross section, human breast

1. INTRODUCTION

Biomedical diffuse optical tomography (DOT) has received significant attention and development in the past two decades and has been applied to image, such as, human breast, infant brain and joints. The state of art diffuse optical tomography currently relies on an iterative image reconstruction approach to construct the optical properties of the interior of the medium. This approach is computationally demanding yet provides limited spatial resolution.¹ Reconstruction of images with adequate spatial resolution and accurate localization and characterization of the inhomogeneities remain a formidable task.

An alternative optical imaging approach is optical imaging using independent component analysis (OPTICA). The principle of OPTICA is to first sort out the signal due to individual inhomogeneity and then perform three dimensional (3D) localization and characterization for each inhomogeneity, using a massive data set generated by a multi-source illumination and multi-detector signal acquisition scheme. Independent component analysis has been extensively applied in fields such as Electroencephalogram (EEG) and functional MRI (fMRI) and shown effective in separating signals from different brain activity centers. Our previous work has shown that such an approach significantly improves the sensitivity to small/weak absorptive, scattering and/or fluorescence inhomogeneities and can achieve a 3D localization of the target with error less than 1mm.

In this paper, we report on a back projection method to obtain high-resolution cross-section images of targets inside highly scattering media, enhancing OPTICA. We demonstrate the performance of OPTICA by imaging a $42 \times 30 \times 33\text{mm}^3$ model human breast assembled using *ex vivo* breast tissues. A $5 \times 5 \times 3\text{mm}^3$ tumor was placed at the midplane. OPTICA located the tumor within $\sim 1\text{mm}$ of its known position. It also identified a 10mm low scattering structure at midplane, and a 3mm low scattering structure near the surface. Subsequent pathological analysis confirmed the tumor, and identified the other two structures as glandular breast tissues. The reconstructed cross section images and optical properties of the targets were consistent with pathology findings.

2. THEORETICAL FORMALISM OF OPTICAL IMAGING USING INDEPENDENT COMPONENT ANALYSIS

The presence of optical inhomogeneities inside a turbid medium perturbs the intensity of emergent light from the medium under illumination by a probing beam. In the diffusion approximation, the change of the light intensity on the boundary of the specimen due to absorptive and scattering objects (inhomogeneities) can be written as:^{2,3}

$$-\Delta I(\mathbf{r}_d, \mathbf{r}_s) = \int d^3\mathbf{r} \delta\mu_a(\mathbf{r}) c G(\mathbf{r}_d, \mathbf{r}) G(\mathbf{r}, \mathbf{r}_s) + \int d^3\mathbf{r} \delta D(\mathbf{r}) c \nabla_{\mathbf{r}} G(\mathbf{r}_d, \mathbf{r}) \cdot \nabla_{\mathbf{r}} G(\mathbf{r}, \mathbf{r}_s) \quad (1)$$

to the first order of Born approximation⁴ when illuminated by a point source of unit power, where \mathbf{r}_s and \mathbf{r}_d are the positions of the probing source and the light detector on the boundary, $\delta\mu_a(\mathbf{r}) = \mu_a(\mathbf{r}) - \mu_{a0}$ and $\delta D(\mathbf{r}) = D(\mathbf{r}) - D_0$ are the differences in absorption coefficient and diffusion coefficient, respectively, between the inhomogeneity at \mathbf{r} and the background, c is the speed of light in the medium, and $G(\mathbf{r}, \mathbf{r}')$ is the Green's function describing light propagation from \mathbf{r}' to \mathbf{r} inside the background turbid medium of absorption and diffusion coefficients μ_{a0} and D_0 .

OPTICA assumes each inhomogeneity within the scattering medium to be a virtual source and express the change of the light intensity on the boundary of the specimen as:

$$-\Delta I(\mathbf{r}_d, \mathbf{r}_s) = \sum_j a_j(\mathbf{r}_d) s_j(\mathbf{r}_s) \quad (2)$$

where $s_j(\mathbf{r}_s)$ represents the j -th inhomogeneity illuminated by the incident wave at \mathbf{r}_s , and $a_j(\mathbf{r}_d)$ is the weighting matrix describing the propagation of light from the j -th inhomogeneity to the detector at \mathbf{r}_d . Each absorptive inhomogeneity contributes one term in Eq. (2) and each scattering inhomogeneity contributes three terms in Eq. (2). The detected change of the light intensity (2) is hence a linear mixture of signals where a_j and s_j can now be interpreted as the j -th weighting matrix and virtual source, respectively. Owing to the statistical independence between these virtual sources, independent component analysis of $-\Delta I$ will yield a list of independent components and recover both a_j and s_j . The number of the leading independent components gives the number of objects. The location and characterization of the j -th target is obtained from the analysis of the retrieved independent component (s_j and a_j) which relates directly to the source-to-object and object-to-detector Green's functions $G(\mathbf{r}_j, \mathbf{r}_s)$ and $G(\mathbf{r}_d, \mathbf{r}_j)$ and the optical property of the target where \mathbf{r}_j is the position of the j -th object.⁵⁻⁸

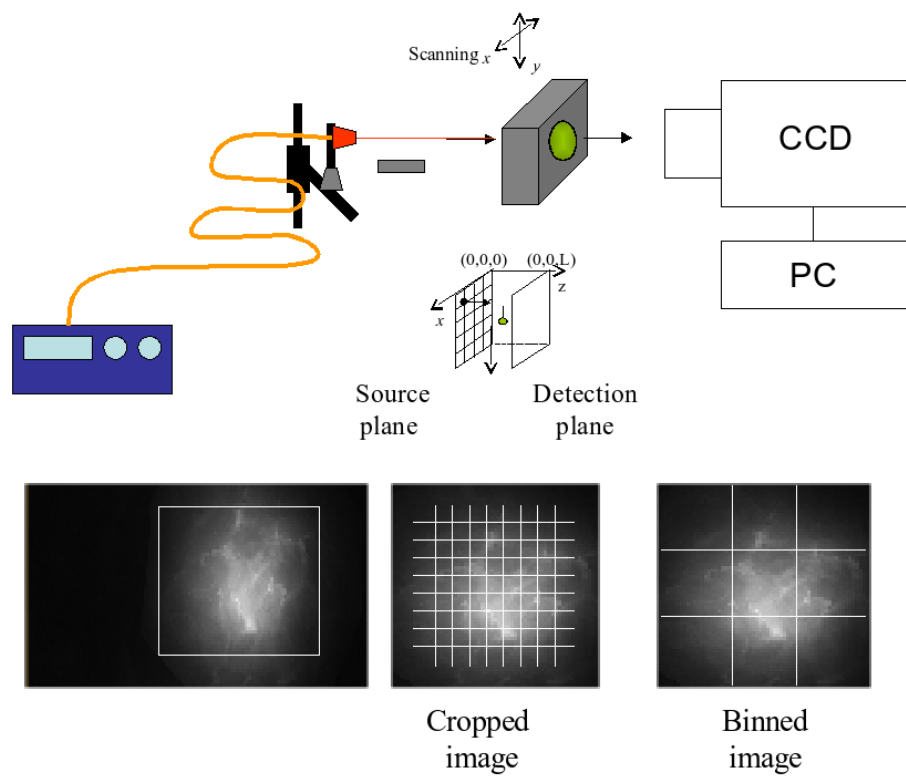
For a slab geometry investigated here, there are three virtual sources of specific patterns (one centrosymmetric and two dumbbell-shaped) associated with one scattering inhomogeneity, whereas only one centrosymmetric virtual source is associated with one absorptive inhomogeneity. Among the three virtual sources associated with one scattering inhomogeneity, the centrosymmetric virtual source is the easiest to detect. The centrosymmetric virtual source and the corresponding weighting matrix are $s_j \propto G(\mathbf{r}_j, \mathbf{r}_s)$ and $a_j \propto G(\mathbf{r}_d, \mathbf{r}_j)$, and $s_j \propto \frac{\partial G}{\partial z}(\mathbf{r}_j, \mathbf{r}_s)$ and $a_j \propto \frac{\partial G}{\partial z}(\mathbf{r}_d, \mathbf{r}_j)$, respectively, for absorptive and scattering inhomogeneities. A simple least square fitting of the centrosymmetric component, such as

$$\min_{\mathbf{r}_j, \alpha_j, \beta_j} \left\{ \sum_{\mathbf{r}_s} [\alpha_j^{-1} s_j(\mathbf{r}_s) - G(\mathbf{r}_j, \mathbf{r}_s)]^2 + \sum_{\mathbf{r}_d} [\beta_j^{-1} a_j(\mathbf{r}_d) - G(\mathbf{r}_d, \mathbf{r}_j)]^2 \right\}. \quad (3)$$

for the absorptive object, can be used to yield the 3D location \mathbf{r}_j and the strength $\alpha_j \beta_j$ of the target. When a prior knowledge about the property of the target is not available, Eq. (3) can still be used to estimate the 3D location of the target regardless absorption or scattering property of the target since $\frac{\partial G}{\partial z}(\mathbf{r}_j, \mathbf{r}_s) \simeq -\kappa G(\mathbf{r}_j, \mathbf{r}_s)$ and $\frac{\partial G}{\partial z}(\mathbf{r}_d, \mathbf{r}_j) \simeq -\kappa G(\mathbf{r}_d, \mathbf{r}_j)$ where $\kappa = \sqrt{(\mu_{a0} - i\omega/c)/D_0}$ chosen to have a nonnegative real part with ω the modulation frequency of the incident wave.

The signal of the j -th target is simply given by $-\Delta I_j = a_j(\mathbf{r}_d) s_j(\mathbf{r}_s)$. On the other hand, the centrosymmetric signal of the j -th target can be approximately expressed as a double convolution in the form of

$$-\Delta I_j(\mathbf{r}_d, \mathbf{r}_s) = \int G(\boldsymbol{\rho}_d - \boldsymbol{\rho}, z_d, z_j) X_j(\boldsymbol{\rho}) G(\boldsymbol{\rho} - \boldsymbol{\rho}_s, z_j, z_s) d\boldsymbol{\rho} \quad (4)$$



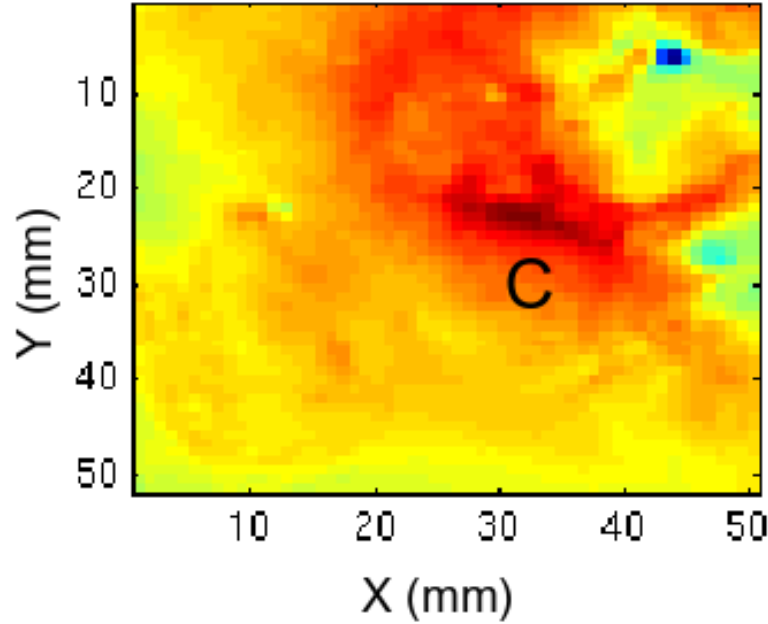


Figure 2. Independent light intensity distributions on the detector plane obtained by OPTICA for the cancer site. The cancer site (C) was found at a depth of 14.8mm .

4. RESULTS

A typical raw image measured on the detector plane at one scanning position is shown in the inset of Fig. 1. The average of all the 22×16 images was used to obtain the optical property of the background medium. The absorption coefficient of the background medium is found to be $\mu_a = 0.0039\text{mm}^{-1}$ assuming the transport mean free path $l_t = 1\text{mm}$. Each raw image is first cropped to retain the region within the window of $42 \times 30\text{mm}^2$ over which image reconstruction would be performed, and binned to enhance the signal-to-noise ratio. All the binned images corresponding to illumination of the grid points in sequence were then stacked, and used as input for independent component analysis.

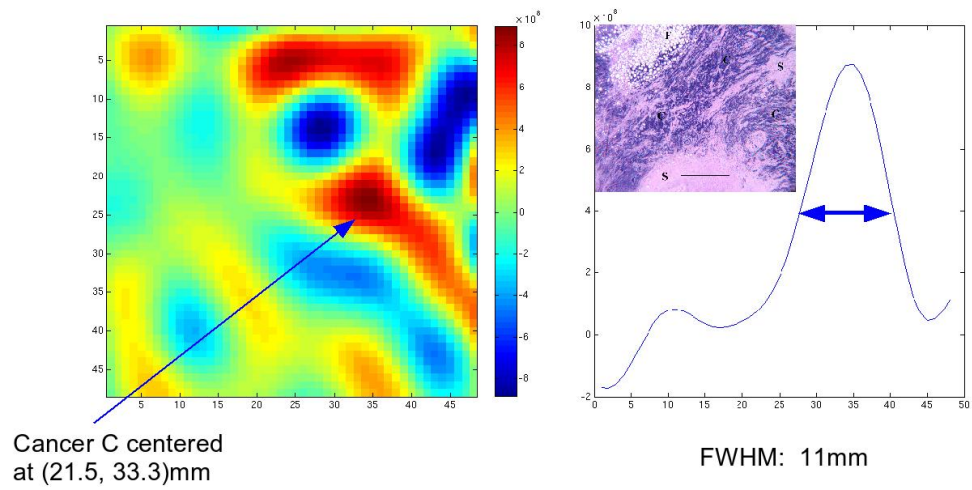
The independent light intensity distributions obtained by OPTICA is displayed in Fig. 2. The cancer site was found at the depth of 14.8mm from fitting the independent light intensity distribution to the background Green's function.

The back-projection of the detected signal for the cancer site (C) produced its cross section images at the depth of 14.8mm in Fig. 3. The corresponding profile along the horizontal direction is displayed on the right for the target. The cancer site is estimated to be 11mm in size and it scatters light more strongly. Representative histology of the site is displayed as the inset.

The investigated *ex vivo* breast sample contained minimal amount of blood and hence the reconstructed images is for the scattering property of the sample. The change of μ'_s for the targets can further be estimated from the reconstructed independent component (s_j and a_j) for the site. It was found site C has enhanced scattering compared to the background (mainly adipose tissue). Subsequent pathological analysis confirmed the site C as tumor.

5. DISCUSSION

The nature of the inhomogeneity (either absorptive or scattering or mixed) can be discovered by OPTICA with CW measurement when the signal to noise ratio is high.^{6,7} When the signal to noise ratio is not favorable, the recovered independent component will be due to both absorption and scattering perturbations at the site of the inhomogeneity. The strength of the inhomogeneity will be proportional to $\delta\mu_a + \kappa^2\delta D = \delta\mu_a + (\mu_{a0} - i\omega/c)\delta D/D_0$. This provides a very simple approach to discriminate absorption vs scattering if multiple modulation frequencies ω are available. The capability of OPTICA separating absorption from scattering inhomogeneities can be significantly improved with a time-domain or frequency domain measurement.



Analytical cumulant solution of the vector radiative transfer equation investigates backscattering of circularly polarized light from turbid media

Wei Cai, Xiaohui Ni, S. K. Gayen, and R. R. Alfano

Institute for Ultrafast Spectroscopy and Lasers, Department of Physics, The City College of City University of New York, New York, New York 10031, USA

(Received 6 April 2006; published 8 November 2006)

The backscattering of circularly polarized light pulses from an infinite uniform scattering medium is studied as a function of helicity of the incident light and size of scatterers in the medium. The approach considers a polarized short pulse of light incident on the scattering medium, and uses an analytical cumulant solution of the vector radiative transfer equation with the phase matrix obtained from the Mie theory to calculate the temporal profile of scattered polarized photons for any position and any angle of detection. The general expression for the scattered photon distribution function is an expansion in spatial cumulants up to an arbitrary high order. Truncating the expansion at the second-order cumulant, a Gaussian analytical approximate expression for the temporal profile of scattered polarized photons is obtained, whose average center position and half width are always exact. The components of scattered light copolarized and cross polarized with that of the incident light can be calculated and used for determining the degree of polarization of the scattered light. The results show that circularly polarized light of the same helicity dominates the backscattered signal when scatterer size is larger than the wavelength of light. For the scatterers smaller than the wavelength, the light of opposite helicity makes the dominant contribution to the backscattered signal. The theoretical estimates are in good agreement with our experimental results.

DOI: [10.1103/PhysRevE.74.056605](https://doi.org/10.1103/PhysRevE.74.056605)

PACS number(s): 42.25.Dd, 42.25.Ja, 42.68.Ay

I. INTRODUCTION

The recent increased interest in the study [1–12] of polarized light propagation through turbid media derives from a variety of practical applications. Polarized light multiple scattered from a turbid medium carries information about the medium interior [13] such as, particle size and concentration, size distribution, and refractive index variation, which can be useful for biomedical imaging [13–15], endoscopic evaluation of biological tissues [16], investigation of biological cell differentiation [17,18], flow cytometry [18,19], lidar-based remote sensing of the atmospheric cloud, aerosol fog and smog [20,21], and imaging of targets in shallow coastal water [22]. Polarization-sensitive imaging has been demonstrated to enhance image contrast of targets embedded in turbid media [14,23].

In particular, it has been observed that for circularly polarized light, randomization of its polarization requires more scattering events than the randomization of its direction [23–27,6,9]. An important consequence of this “polarization memory” [25] is higher resolution and contrast of transillumination images recorded with copolarized light than those recorded with unpolarized or cross-polarized light. Another interesting feature is the dependence of the intensity of the backscattered copolarized and cross-polarized light on the size of the scatterers in the medium [23]. The backscattered light is dominated by light of helicity opposite to that of the incident light if the size of the scatterers is smaller than the wavelength of light. The light of the same helicity dominates when scatterers are larger than the light wavelength. These results have important consequences in the design considerations of imaging systems using backscattered light such as, endoscopic systems. All these developments make it impera-

tive that theoretical formalisms be developed to provide a quantitative explanation of the experimental results, and guidance for the design of imaging systems using polarized light.

Theoretical studies of polarized light propagation through a scattering medium commonly starts with the vector radiative transfer equation (VRTE) [1], and because of the inherent complexity of the problem, a limited number of studies are available to date. A majority of these studies focused on developing numerical solutions of the VRTE. Ishimaru and co-workers first investigated the propagation of continuous wave (CW), polarized wave normally incident on a medium with discrete scatterers using discrete ordinate methods to solve VRTE [2,3]. More recently, they extended the formalism to numerically solve the time-dependent VRTE to account for the propagation of polarized pulses [4]. Kim and Moscoso studied the propagation of a linearly polarized or circularly polarized continuous plane wave normally incident on a plane-parallel medium containing a random distribution of dielectric spheres, and numerically solved the one-dimensional VRTE using a Chebyshev spectral method [5]. The approach was subsequently modified to study the backscattering of circularly polarized plane-wave pulses [6]. Valion *et al.* [7] used a vector Monte Carlo method to study polarized light transport through a semitransparent medium filled with scattering particles. Jiang *et al.* [8] developed a multilayer radiative transfer model that takes into account the state of polarization using the doubling-adding method for passive atmospheric remote sensing applications. More recently, Sakami and Dogariu [9] investigated the propagation of a polarized plane-wave pulse incident at any angle in a random medium using the discrete-ordinates method to

solve the VRTE, and used an angular analysis to obtain details of the polarization flip of circular polarized light. The problem of light scattering and radiative transfer in scattering media and its application to geophysical optics, image transfer, remote sensing, and inverse problems are discussed in the monograph by Kokhanovsky [10].

In this paper, we use the analytical solution of the time-dependent VRTE to compute backscattering of circularly polarized light in an infinite uniform scattering medium. It builds on the analytical cumulant approach for solving the time-dependent radiative transfer equation in an infinite uniform medium that we developed [28–30]. In this approach an arbitrary phase function, as long as it is a function of scattering angle, can be treated. We have derived the exact expression of spatial cumulants of photon distribution at any angle and any time, up to an arbitrary high order. The exact first spatial cumulant represents the center of the distribution and the exact second spatial cumulant represents the width of the distribution. The method of the analytical cumulant solution for the scalar radiative transfer equation can be extended to the vector (polarized) case [31]. In the analytical solution of VRTE, a transform to the circular representation from the Stokes representation of polarization is introduced, and the generalized spherical functions are used for angular expansion, instead of the standard spherical functions for solving the scalar radiative transfer equation. The expressions for the exact first and second spatial cumulants of polarized components as functions of angle \mathbf{s} and time t is derived. Then, intensity of the polarized light is presented by a Gaussian spatial distribution. We apply this method to calculate the backscattering of circular polarized light in a scattering medium. The results show that circularly polarized light of the same helicity dominates the backscattered signal when scatterer size is larger than the wavelength of light. For the scatterers smaller than the wavelength, light of opposite helicity makes the dominant contribution to the backscattered signal. The theoretical conclusion is in good agreement with our experimental results [23].

The paper is organized as follows. In Sec. II we review the analytical solution of VRTE. In Sec. III, the numerical results are presented and are compared with experiments. Section IV is devoted to discussion and conclusion.

II. THEORETICAL FORMALISM

A. Polarized components of light

In the Stokes polarization representation [32] (SP), the polarized light is described by $\mathbf{I}^{SP} = [I, Q, U, V]$. The polarized components of distribution we will study are the parallel component $I_{\parallel} = (I + Q)/2$, the perpendicular component $I_{\perp} = (I - Q)/2$, the right-circular component $I_R = (I + V)/2$, and the left-circular component $I_L = (I - V)/2$, since these quantities are positive definite, and are experimentally measurable.

The vector radiative transfer equation for the polarized photon distribution function $\mathbf{I}(\mathbf{r}, \mathbf{s}, t)$ in an infinite uniform medium, illuminated by a point light source providing short pulse, $\mathbf{I}^{(0)} \delta(\mathbf{r} - \mathbf{r}_0) \delta(\mathbf{s} - \mathbf{s}_0) \delta(t - 0)$ is given by [33]

$$\begin{aligned} & \partial \mathbf{I}(\mathbf{r}, \mathbf{s}, t) / \partial t + c \mathbf{s} \cdot \nabla_{\mathbf{r}} \mathbf{I}(\mathbf{r}, \mathbf{s}, t) + \mu_a \mathbf{I}(\mathbf{r}, \mathbf{s}, t) \\ &= \mu_s \int \mathbf{P}(\mathbf{s}, \mathbf{s}') [\mathbf{I}(\mathbf{r}, \mathbf{s}', t) - \mathbf{I}(\mathbf{r}, \mathbf{s}, t)] d\mathbf{s}' \\ &+ \mathbf{I}^{(0)} \delta(\mathbf{r} - \mathbf{r}_0) \delta(\mathbf{s} - \mathbf{s}_0) \delta(t - 0), \end{aligned} \quad (1)$$

where vector $\mathbf{I}(\mathbf{r}, \mathbf{s}, t)$ has four polarization components, c is the light speed in the medium, μ_s is the scattering rate, μ_a is the absorption rate, and $\mathbf{P}(\mathbf{s}, \mathbf{s}')$ is the 4×4 phase matrix. A meridian plane parallel to the z axis and the light direction \mathbf{s} , is used as a plane of reference for the description of the polarization state. In SP the components Q, U vary with the rotation of the reference plane around the light propagation direction. With a rotation of reference plane through an angle $\alpha \geq 0$ (in the counterclockwise direction, when looking in the direction of propagation) \mathbf{I}^{SP} varies as $(\mathbf{I}')^{SP} = \mathbf{L}(\alpha) \mathbf{I}^{SP}$, where $\mathbf{L}(\alpha)$ is given by

$$\mathbf{L}(\alpha) = \begin{bmatrix} 1 & 0 & 0 & 0 \\ 0 & \cos 2\alpha & \sin 2\alpha & 0 \\ 0 & -\sin 2\alpha & \cos 2\alpha & 0 \\ 0 & 0 & 0 & 1 \end{bmatrix}. \quad (2)$$

When light propagates along the z direction, Q, U vary with the change of the azimuthal angle ϕ .

The phase matrix in the fixed coordinates is given by:

$$\mathbf{P}(\mathbf{s}, \mathbf{s}') = \mathbf{L}(\pi - \chi) \mathbf{P}(\cos \Theta) \mathbf{L}(-\chi'), \quad (3)$$

where Θ is the angle between light rays before and after scattering in the scattering plane, and the matrices $\mathbf{L}(-\chi')$ and $\mathbf{L}(\pi - \chi)$ are those required to rotate meridian planes before and after scattering onto a local scattering plane. The intrinsic property of a scattering mechanism is described by the 4×4 scattering function $\mathbf{P}(\cos \Theta)$, which is assumed to depend only on $\cos \Theta = \mathbf{s} \cdot \mathbf{s}'$. It is convenient to use a representation of the polarized light in which $\mathbf{L}(\alpha)$ is diagonal, rather than Eq. (2). A circular polarization representation (CP), first proposed by Kuščer and Ribarič [34] and presented by Hovenier and van der Mee [35], is $\mathbf{I}^{CP} = [I_2, I_0, I_{-0}, I_{-2}]$, where $I_0 = (I + V)/2$, $I_{-0} = (I - V)/2$, $I_2 = (Q + iU)/2$, and $I_{-2} = (Q - iU)/2$, or $\mathbf{I}^{CP} = \mathbf{T} \mathbf{I}^{SP}$, with

$$\mathbf{T} = \frac{1}{2} \begin{bmatrix} 0 & 1 & i & 0 \\ 1 & 0 & 0 & 1 \\ 1 & 0 & 0 & -1 \\ 0 & 1 & -i & 0 \end{bmatrix} \text{ and } \mathbf{T}^{-1} = \begin{bmatrix} 0 & 1 & 1 & 0 \\ 1 & 0 & 0 & 1 \\ -i & 0 & 0 & i \\ 0 & 1 & -1 & 0 \end{bmatrix}. \quad (4)$$

In CP a rotation of the reference plane through an angle α around the light direction causes I_m^{CP} to be multiplied by $\exp(-im\alpha)$, $m=2, 0, 0, -2$. Notice that I_0 and I_{-0} actually have the same rotational property. For the phase matrix, transform between two representations is $\mathbf{P}^{CP} = \mathbf{T} \mathbf{P}^{SP} \mathbf{T}^{-1}$.

In CP it is convenient to expand the phase matrix \mathbf{P}^{CP} using the generalized spherical functions (GSF). The generalized spherical functions $P_{mn}^l(\beta)$ are related to the $d_{mn}^l(\beta)$

in the angular momentum theory [36] by $P_{m,n}^l(\beta) = (i)^{m-n} d_{mn}^l(\beta)$. In the Appendix, the expressions for $d_{mn}^l(\beta)$ are presented.

B. Phase matrix using Mie theory

Elements of the CP phase matrix in the scattering plane, $P_{mn}^{CP}(\cos \Theta)$ can be expanded by GSF;

$$P_{mn}^{CP}(\cos \Theta) = \frac{1}{4\pi} \sum_l \rho_{mn}^l P_{m,n}^l(\cos \Theta), \quad (5)$$

with $m, n=2, 0, -0, -2$, and $l \geq \max(|m|, |n|)$. The coefficients ρ_{mn}^l provide a description of the scattering mechanism. In most useful cases, the coefficients ρ_{mn}^l have properties: (i) $\rho_{mn}^l = \rho_{m,-m}^l$ are real; (ii) $\rho_{mn}^l = \rho_{nm}^l = \rho_{-m,-n}^l$; (iii) $\rho_{20}^l = [\rho_{2-0}^l]^*$ (* means complex conjugate). Therefore, for each $l \geq 2$, there are six independent real elements: $\rho_{00}^l, \rho_{22}^l, \rho_{0-0}^l, \rho_{2-2}^l, \text{Re}[\rho_{20}^l]$, and $\text{Im}[\rho_{20}^l]$. For $l=0, 1$, only ρ_{00}^l and ρ_{0-0}^l are nonzero. These numerical coefficients can be calculated using the Mie theory for a spherical particle. We have $\rho_{00}^l = (\alpha_1' + \alpha_4')/2$, $\rho_{0-0}^l = (\alpha_1' - \alpha_4')/2$, $\rho_{22}^l = (\alpha_2' + \alpha_3')/2$, $\rho_{2-2}^l = (\alpha_2' - \alpha_3')/2$, $\text{Re}[\rho_{20}^l] = \beta_1'$, $\text{Im}[\rho_{20}^l] = \beta_2'$, where the coefficients $\alpha_{1,2,3,4}'$ and $\beta_{1,2}'$ are formulated in Eqs. (4.81)–(4.86) in Ref. [37].

C. Photon angular distribution $\mathbf{F}(\mathbf{s}, \mathbf{s}_0, t)$

When we make a spherical harmonics expansion of Eq. (1), the difficulty is that the term $c\mathbf{s} \cdot \nabla_{\mathbf{r}} \mathbf{I}(\mathbf{r}, \mathbf{s}, t)$ couples equations of different harmonics. We first study the photon distribution in the angular space in CP initially incident along \mathbf{s}_0 ,

$$\mathbf{F}(\mathbf{s}, \mathbf{s}_0, t) = \int \mathbf{I}(\mathbf{r}, \mathbf{s}, t) d\mathbf{r}, \quad (6)$$

where integration is over the whole space. Evaluation of the integral in Eq. (6) over Eq. (1) leads to

$$\begin{aligned} & \partial \mathbf{F}(\mathbf{s}, \mathbf{s}_0, t) / \partial t + \mu_a \mathbf{F}(\mathbf{s}, \mathbf{s}_0, t) \\ & + \mu_s \left[\mathbf{F}(\mathbf{s}, \mathbf{s}_0, t) - \int \mathbf{P}(\mathbf{s}, \mathbf{s}') \mathbf{F}(\mathbf{s}', \mathbf{s}_0, t) d\mathbf{s}' \right] \\ & = \mathbf{I}^{(0)} \delta(\mathbf{s} - \mathbf{s}_0) \delta(t - 0). \end{aligned} \quad (7)$$

The gradient term disappears in Eq. (7) because of the Gauss-Stokes law. Hence, $\mathbf{F}(\mathbf{s}, \mathbf{s}_0, t)$ can be exactly solved by expanding in GSF's. When \mathbf{s}_0 is set along the z direction, the initial polarization state is set as n_0 , and the initial reference plane is set as the x - z plane, we have

$$\begin{aligned} F_{mn_0}(\mathbf{s}, \mathbf{s}_0, t) = & \sum_l \left[F_{mn_0}^l(t) P_{m,n_0}^l(\cos \theta) \right. \\ & \left. - \delta_{m,n_0} \frac{2l+1}{4\pi} e^{-\mu_s t} P_{0,0}^l(\cos \theta) \right] \\ & \times \exp(-in_0 \phi) \exp(-\mu_a t), \end{aligned} \quad (8)$$

where $\mathbf{s} = (\theta, \phi)$, and $m, n_0 = 2, 0, -0, -2$, $l \geq \max(|m|, |n_0|)$. The second term in Eq. (8) represents the ballistic (unscattered) component of photons. $F_{mn_0}^l(t)$ in Eq. (8) is the solution of the equation

$$dF_{mn_0}^l(t)/dt = \sum_n \Pi_{mn}^l F_{mn_0}^l(t), \quad (9)$$

under the initial condition

$$F_{mn_0}^l(t=0) = \delta_{m,n_0} (2l+1)/4\pi, \quad (10)$$

where $\Pi_{mn}^l = \mu_s [\delta_{m,n} - \rho_{mn}^l / (2l+1)]$. The solution $F_{mn_0}^l(t)$ has the following form:

$$F_{mn_0}^l(t) = \frac{2l+1}{4\pi} \sum_i [B_{mn_0}^l]_i \exp(-\lambda_i^l t), \quad (11)$$

$i=1, 2, 3, 4$ for $l \geq 2$, and $i=1, 2$ for $l=1, 2$. The eigenvalues λ_i^l for $l \geq 2$ is given by

$$\begin{aligned} \lambda_i^l = (1/2) & \left\{ (\Pi_{00}^l + \Pi_{22}^l \pm \Pi_{0-0}^l \pm \Pi_{2-2}^l) \right. \\ & + \left[(\Pi_{00}^l - \Pi_{22}^l \pm \Pi_{0-0}^l \mp \Pi_{2-2}^l)^2 \right. \\ & \left. \left. \pm 16 \left(\frac{\text{Re}[\Pi_{20}^l]}{\text{Im}[\Pi_{20}^l]} \right)^2 \right]^{1/2} \right\}, \end{aligned} \quad (12)$$

for $i=1, 2$, and for $i=3, 4$, the sign + before the square brackets in Eq. (12) is replaced by $-$. For $l=0, 1$ two eigenvalues are $\lambda_i^l = \Pi_{00}^l \pm \Pi_{0-0}^l$. The constant coefficients $[B_{mn_0}^l]_i$ can be determined using linear algebra under the initial condition Eq. (10) [31].

In SP the angular distribution component of $I_m = [I, Q, U, V]$, with the initial polarized state $\mathbf{I}^{SP(0)}$, is obtained by

$$F_m^{SP}(\mathbf{s}, \mathbf{s}_0, t) = [\mathbf{T}^{-1} \mathbf{F}(\mathbf{s}, \mathbf{s}_0, t) \mathbf{T} \mathbf{I}^{SP(0)}]_m. \quad (13)$$

The angular distribution for the parallel polarized component is given by $F_{\parallel}(\mathbf{s}, \mathbf{s}_0, t) = [F_I^{SP}(\mathbf{s}, \mathbf{s}_0, t) + F_Q^{SP}(\mathbf{s}, \mathbf{s}_0, t)]/2$. Similarly, we have $F_{\perp} = (F_I^{SP} - F_Q^{SP})/2$, $F_R = (F_I^{SP} + F_V^{SP})/2$, and $F_L = (F_I^{SP} - F_V^{SP})/2$.

D. The cumulant expansion

The polarized photon distribution $I_m(\mathbf{r}, \mathbf{s}, t)$ in an infinite uniform medium can be written as [31]

$$I_m(\mathbf{r}, \mathbf{s}, t) = \left\langle \delta \left(\mathbf{r} - c \int_0^t \mathbf{s}(t') dt' \right) \delta[\mathbf{s}(t) - \mathbf{s}] \right\rangle_m, \quad (14)$$

where $\langle \cdots \rangle$ means the ensemble average in the angular space. We perform a Fourier transform of the first δ function, then make a cumulant expansion, and obtain

$$I_m(\mathbf{r}, \mathbf{s}, t) = F_m(\mathbf{s}, \mathbf{s}_0, t) \frac{1}{(2\pi)^3} \int d\mathbf{q} \exp \left\{ i\mathbf{q} \cdot \mathbf{r} + \sum_{k=1}^{\infty} \frac{(-ic)^k}{k!} \sum_{j_k} \cdots \sum_{j_1} q_{j_k} \cdots q_{j_1} \times \left[\left\langle \int_0^t dt_k \cdots \int_0^t dt_1 T[s_{j_k}(t_k) \cdots s_{j_1}(t_1)] \right\rangle_c \right]_m \right\}, \quad (15)$$

where T denotes time-ordered multiplication [38], and the subscript-index c denotes cumulant. The cumulants are related to the moments. For an arbitrary random variable A , we have $\langle A \rangle_c = \langle A \rangle$, $\langle A^2 \rangle_c = \langle A^2 \rangle - \langle A \rangle \langle A \rangle$, and so on. The corresponding moment can be estimated using a standard time-dependent Green's-function approach, which is given by

$$\begin{aligned} & \left[\left\langle \int_0^t dt_k \cdots \int_0^t dt_1 T[s_{j_k}(t_k) \cdots s_{j_1}(t_1)] \right\rangle \right]_m \\ &= \frac{1}{F_m(\mathbf{s}, \mathbf{s}_0, t)} \left\{ \left[\int_0^t dt_k \int_0^{t_k} dt_{k-1} \cdots \int_0^{t_2} dt_1 \int d\mathbf{s}^{(k)} \right. \right. \\ & \quad \times \int d\mathbf{s}^{(k-1)} \cdots \int d\mathbf{s}^{(1)} \mathbf{F}(\mathbf{s}, \mathbf{s}^{(k)}, t - t_k) s_{j_k}^{(k)} \\ & \quad \times \mathbf{F}(\mathbf{s}^{(k)}, \mathbf{s}^{(k-1)}, t_k - t_{k-1}) s_{j_{k-1}}^{(k-1)} \cdots \mathbf{F}(\mathbf{s}^{(2)}, \mathbf{s}^{(1)}, t_2 - t_1) s_{j_1}^{(1)} \\ & \quad \left. \left. \times \mathbf{F}(\mathbf{s}^{(1)}, \mathbf{s}_0, t_1 - 0) \mathbf{I}^{(0)} \right]_m + (\text{perm}) \right\}, \quad (16) \end{aligned}$$

where the abbreviation “perm” means all $k! - 1$ terms obtained by permutation of $\{j_i\}$, $i = 1, \dots, k$ from the first term, and $\mathbf{F}(\mathbf{s}^{(i)}, \mathbf{s}^{(i-1)}, t_i - t_{i-1})$ is the exact solution given by Eq. (8) in Sec. II C. If we cut off the summation in Eq. (15) at $k = 2$, the integration leads to a Gaussian spatial distribution characterized by the first and second cumulants.

1. First cumulant (center of the spatial distribution)

In CP it is convenient to set \mathbf{s} in a spherical harmonic basis,

$$\mathbf{s} = [s_1, s_0, s_{-1}] = [-2^{-1/2} \sin \theta e^{+i\phi}, \cos \theta, +2^{-1/2} \sin \theta e^{-i\phi}], \quad (17)$$

which is related to Cartesian component basis $\alpha = x, y, z$ by $s_\alpha = \sum U_{\alpha j} s_j$, $j = 1, 0, -1$ with

$$U = 2^{-1/2} \begin{bmatrix} -1 & 0 & 1 \\ i & 0 & i \\ 0 & 2^{1/2} & 0 \end{bmatrix}. \quad (18)$$

Using the recurrence relation and the orthogonality relation of GSF, the unnormalized first moment in CP, when \mathbf{s}_0 is along the z direction, is obtained;

$$\begin{aligned} \langle \mathbf{R}_j \rangle_{mn_0} &= c \int_0^t dt' \int d\mathbf{s}' \sum_n F_{mn}(\mathbf{s}, \mathbf{s}', t - t') s'_j F_{mn_0}(\mathbf{s}', \mathbf{s}_0, t') \\ &= c \sum_l \left\{ P_{m, n_0 - j}^l (\cos \theta) e^{-i(n_0 - j)\phi} \gamma_j \sum_n \sum_h \frac{2(l - h) + 1}{4\pi} \right. \\ & \quad \times D_{m, n, n_0}^{l, h}(t) \langle l - h, 1, n, 0 | l, n \rangle \langle l - h, 1, n_0, -j | l, n_0 - j \rangle \\ & \quad \left. - \delta_{j,0} \delta_{m, n_0} \frac{2l + 1}{4\pi} t e^{-\mu_s t} P_{0,0}^l (\cos \theta) e^{-in_0 \phi} \right\}, \quad (19) \end{aligned}$$

with $\gamma_{\pm 1} = \mp i$, $\gamma_0 = 1$, $\langle l_1, l_2, m_1, m_2 | L, M \rangle$ is Clebsch-Gordan coefficients in angular momentum theory [36], presented in the Appendix, and

$$\begin{aligned} D_{m, n, n_0}^{l, h}(t) &= \sum_{i, j} [B_{mn}^l]_i [B_{nn_0}^{l-h}]_j \left(\frac{\exp(-\lambda_j^{l-h} t) - \exp(-\lambda_i^l t)}{\lambda_i^l - \lambda_j^{l-h}} \right) \\ & \quad \times \exp(-\mu_a t), \quad (20) \end{aligned}$$

where $i, j = 1, 2, 3, 4$ for $l \geq 2$, and $i, j = 1, 2$ for $l = 1, 2$.

In SP the component of the unnormalized first moment of $I_m = [I, Q, U, V]$, with the initial polarized state $\mathbf{I}^{SP(0)}$, and $\alpha = x, y, z$, is obtained by

$$\langle \mathbf{R}_\alpha \rangle_m^{SP} = \sum_j U_{\alpha j} [\mathbf{T}^{-1} \langle \mathbf{R}_j \rangle \mathbf{T} \mathbf{I}^{SP(0)}]_m. \quad (21)$$

The center of photon distribution for the linearly polarized components is obtained by

$$R_{p, \alpha}^c(\mathbf{s}, t) = \frac{[\langle \mathbf{R}_\alpha \rangle_I^{SP} \pm \langle \mathbf{R}_\alpha \rangle_Q^{SP}]}{2F_p(\mathbf{s}, \mathbf{s}_0, t)}, \quad (22)$$

where the $+$ sign holds for the $p = \parallel$ component, and the $-$ sign holds for the $p = \perp$ component. The center of photon distribution for the circularly polarized components is obtained by

$$R_{c, \alpha}^c(\mathbf{s}, t) = \frac{[\langle \mathbf{R}_\alpha \rangle_I^{SP} \pm \langle \mathbf{R}_\alpha \rangle_V^{SP}]}{2F_c(\mathbf{s}, \mathbf{s}_0, t)}, \quad (23)$$

where the $+$ sign holds for the $c = R$ component, and the $-$ sign holds for the $c = L$ component.

2. Second cumulant (width of the spatial distribution)

Similarly, we can obtain the expression for the unnormalized second moment in CP,

$$\begin{aligned}
\langle \mathbf{R}_{j_2} \mathbf{R}_{j_1} \rangle_{mn_0} = c^2 \sum_l \left\{ P_{m,n_0-j_1-j_2}^l (\cos \theta) e^{-i(n_0-j_1-j_2)\phi} \gamma_{j_2} \gamma_{j_1} \sum_{n_2} \sum_{n_1} \sum_{h_2} \sum_{h_1} \frac{2(l-h_2-h_1)+1}{4\pi} \right. \\
\times E_{m,n_2,n_1,n_0}^{l,h_2,h_1}(t) \langle l-h_2, 1, n_2, 0 | l, n_2 \rangle \langle l-h_2, 1, n_0-j_1, -j_2 | l, n_0-j_1-j_2 \rangle \langle l-h_2-h_1, 1, n_1, 0 | l-h_2, n_1 \rangle \\
\left. \times \langle l-h_2-h_1, 1, n_0, -j_1 | l-h_2, n_0-j_1 \rangle - \delta_{j_2,0} \delta_{j_1,0} \delta_{m,n_0} \frac{2l+1}{4\pi} \frac{t^2}{2} e^{-\mu_s t} P_{0,0}^l (\cos \theta) e^{-in_0\phi} \right\}, \quad (24)
\end{aligned}$$

with

$$\begin{aligned}
E_{m,n_2,n_1,n_0}^{l,h_2,h_1}(t) = \sum_{i,j,f} [B_{mn_2}^l] [B_{n_2 n_1}^{l-h_2}] [B_{n_1 n_0}^{l-h_2-h_1}]_f \exp(-\mu_a t) \\
\times \left(\frac{\exp(-\lambda_f^{l-h_2-h_1} t) - \exp(-\lambda_i^l t)}{(\lambda_j^{l-h_2} - \lambda_f^{l-h_2-h_1})(\lambda_i^l - \lambda_f^{l-h_2-h_1})} \right. \\
\left. - \frac{\exp(-\lambda_j^{l-h_2} t) - \exp(-\lambda_i^l t)}{(\lambda_j^{l-h_2} - \lambda_f^{l-h_2-h_1})(\lambda_i^l - \lambda_j^{l-h_2})} \right), \quad (25)
\end{aligned}$$

where $i, j, f = 1, 2, 3, 4$ for $l \geq 2$, and $i, j, f = 1, 2$ for $l = 1, 2$.

In SP the component of the unnormalized second moment of $I_m = [I, Q, U, V]$, with the initial polarized state $\mathbf{I}^{SP(0)}$, is obtained by

$$\begin{aligned}
\langle \mathbf{R}_\alpha \mathbf{R}_\beta \rangle_m^{SP} = \sum_{j_1} \sum_{j_2} \frac{1}{2} (U_{\alpha j_1} U_{\beta j_2} + U_{\alpha j_2} U_{\beta j_1}) \\
\times [\mathbf{T}^{-1} \langle \mathbf{R}_{j_2} \mathbf{R}_{j_1} \rangle \mathbf{T} \mathbf{I}^{SP(0)}]_m. \quad (26)
\end{aligned}$$

The square of the width of the photon distribution for the linearly polarized component is determined by

$$D_{p,\alpha\beta}(\mathbf{s}, t) = \frac{[\langle \mathbf{R}_\alpha \mathbf{R}_\beta \rangle_I^{SP} \pm \langle \mathbf{R}_\alpha \mathbf{R}_\beta \rangle_Q^{SP}]}{2F_{\parallel}(\mathbf{s}, \mathbf{s}_0, t)} - \frac{1}{2} R_{p,\alpha}^c R_{p,\beta}^c, \quad (27)$$

where the $+$ sign holds for the $p = \parallel$ component, and the $-$ sign holds for the $p = \perp$ component. The square of the width of photon distribution for the circularly polarized components is obtained by

$$D_{c,\alpha\beta}(\mathbf{s}, t) = \frac{[\langle \mathbf{R}_\alpha \mathbf{R}_\beta \rangle_I^{SP} \pm \langle \mathbf{R}_\alpha \mathbf{R}_\beta \rangle_V^{SP}]}{2F_c(\mathbf{s}, \mathbf{s}_0, t)} - \frac{1}{2} R_{c,\alpha}^c R_{c,\beta}^c, \quad (28)$$

where the $+$ sign holds for the $c = R$ component, and the $-$ sign holds for the $c = L$ component.

F. Gaussian distribution of the polarized light

Polarized photon intensity $I_\nu(\mathbf{r}, \mathbf{s}, t)$, $\nu = \parallel, \perp, R, L$, is expressed by an approximate Gaussian distribution,

$$\begin{aligned}
I_\nu(\mathbf{r}, \mathbf{s}, t) = \frac{F_\nu(\mathbf{s}, \mathbf{s}_0, t)}{(4\pi)^{3/2}} \frac{1}{[\det D_\nu]^{1/2}} \exp \left\{ \sum_{\alpha\beta} -\frac{1}{4} [(D_\nu)^{-1}]_{\alpha\beta} \right. \\
\left. \times (r_\alpha - R_{\nu,\alpha}^c)(r_\beta - R_{\nu,\beta}^c) \right\}. \quad (29)
\end{aligned}$$

The ballistic component has been subtracted in the expressions for the angular distribution Eq. (8), for the first cumulant Eq. (19), and for the second cumulant, Eq. (24). This subtraction ensures that the summation over l converges even at very early times, as discussed in Sec. III of Ref. [30].

In the case of the transmission of light, the formalism produces the correct first and second cumulants, but the Gaussian-shaped distribution obtained for early times violates causality, as manifested by the photons at the front edge of the distribution traveling faster than the speed of light in free space. We have introduced an approach to reshape the distribution in Ref. [30], which maintains the correct center position and width of spread of the distribution, and satisfies the causality condition. This technique can be extended to include polarization, combining the formula for the calculation of cumulants of polarized components, in the study of transmission of linear and circular polarized light.

III. RESULT

A. Theoretical result

We now use the formalism developed in Sec. II to study backscattering of circularly polarized light in a scattering medium. A right circularly polarized beam of light with initial Stokes parameters $I = [1, 0, 0, 1]$ and wavelength $\lambda = 610$ nm is assumed to be injected into an infinite medium comprised of polystyrene spheres (with refractive index $m = 1.59$) suspended in water (with refractive index $m_0 = 1.33$). The absorption coefficient of light in the medium is assumed to be zero. The light is incident along the z axis from the origin $(x, y, z) = (0, 0, 0)$. The backscattered light is received by a detector located at $(x_d, 0, 0)$. Figure 1 shows the computed time-resolved profiles of circularly polarized backscattered light as a function of time t (in a unit of l_{tr}/c), collected at direction $\theta = 180^\circ$ and position $x_d = 0.5l_{tr}$, where l_{tr} is the transport mean free path, for polystyrene spheres of diameter (a) $d = 0.10 \mu\text{m}$, (b) $d = 0.213 \mu\text{m}$, (c) $d = 0.855 \mu\text{m}$, and (d) $d = 8.0 \mu\text{m}$. A remarkable feature is that the backscattered signal is dominated by the left circular polarized (LCP) light if the size of scatterers is small compared to the wavelength of light, as shown in Figs. 1(a) and 1(b), but it is dominated by the right circular polarized (RCP) light if the size of scatterers is large, as displayed in Figs. 1(c) and 1(d). Figure 2 shows how the peak intensity of RCP light and LCP light vary with the size of scatterers.

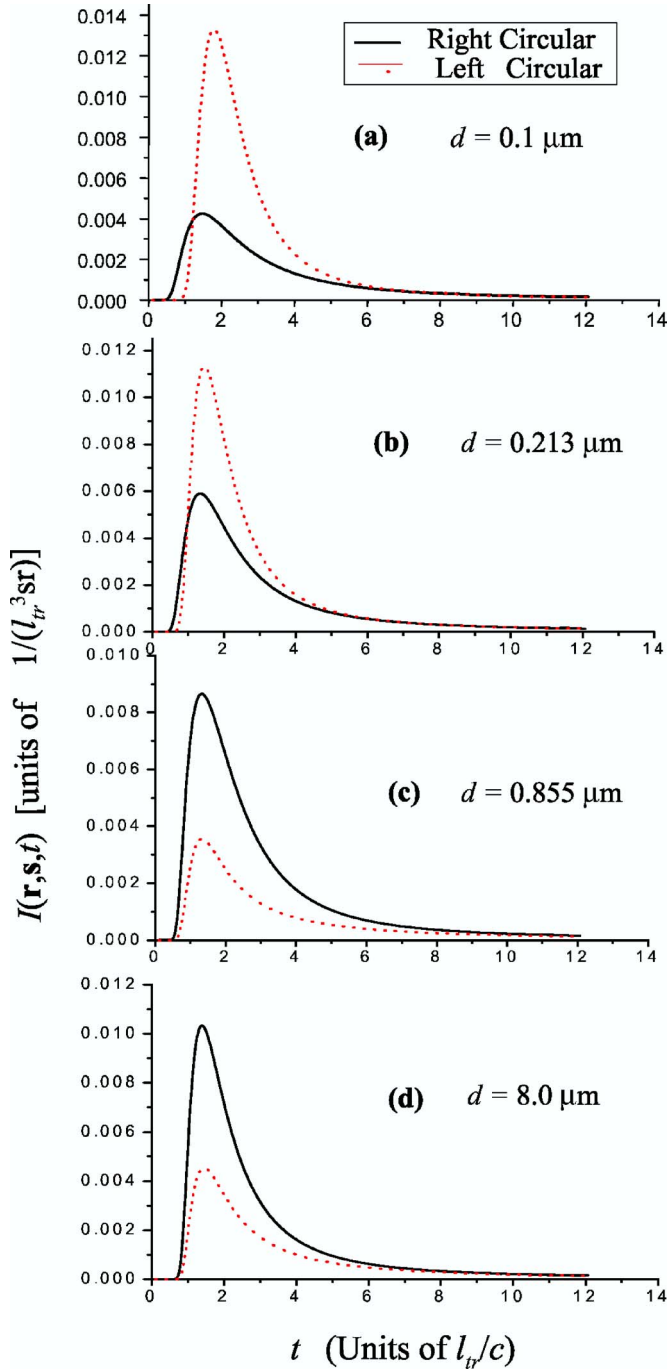


FIG. 1. (Color online) Time-resolved profiles of RCP (solid curve) and LCP (dotted curve) backscattered light intensity as functions of time t (in the unit of l_{tr}/c), received at angle $\theta=180^\circ$ and detector position $x_d=0.5l_{tr}$, where l_{tr} is the transport mean free path, for different diameters of scatterers: (a) $d=0.10\ \mu\text{m}$, (b) $d=0.213\ \mu\text{m}$, (c) $d=0.855\ \mu\text{m}$, and (d) $d=8.0\ \mu\text{m}$. The initial Stokes parameters $\mathbf{I}=[1,0,0,1]$ represent a RCP light beam incident along the z direction, and the wavelength $\lambda=610\ \text{nm}$.

We explain this phenomenon by considering the effect of Mie single scattering together with the effect of multiple scattering. The Mie formula indicates that when $m/m_0=1.19$, for small particles the Stokes V component is negative for θ larger than 90° , which means that the helicity of

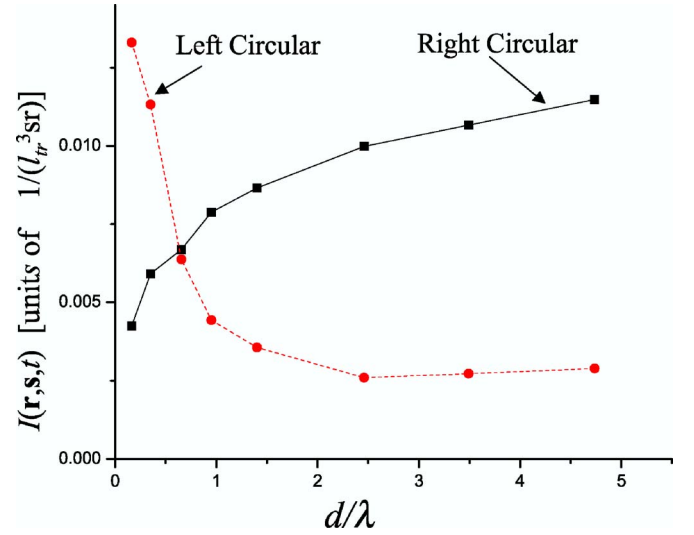


FIG. 2. (Color online) The peak intensity of the time-resolved profile of RCP and LCP backscattered light as functions of d/λ , at angle $\theta=180^\circ$ and detector position $x_d=0.5l_{tr}$. The incident beam is RCP.

light singly backscattered from a small particle will flip. As the particle size increases, the helicity of the near-backward scattered light computed using Mie formula becomes oscillating, and the region of negative V squeezes to a range near $\theta=180^\circ$. For near-forward scattering, the value of V is positive, hence, the helicity does not flip. For large particles the anisotropy factor g is large, and the probability of near-forward scattering is high. For large particles compared to λ , backscattering results from the accumulated effect of many small-angle (near-forward) scattering events, each of which changes the direction only slightly. These small-angle scattering events do not change the helicity of circularly polarized light. Hence, the backscattered light is dominated by the component that maintains the original helicity. When particles are small, however, the events with large-angle scattering play a more important role. The backscattered light is dominated by the component with the flipped helicity.

In view of the above explanation, it is expected that circularly polarized light with reversed helicity dominates only when the detector is located close to the source. When the distance between the source and the detector becomes large, more backscattered photons come from the accumulation of many small-angle scattering events, and those retain the original helicity. Figure 3 shows the computed time-resolved profiles at different source-detector distances: (a) $x_d=0.1l_{tr}$, (b) $x_d=0.2l_{tr}$, (c) $x_d=1.0l_{tr}$ for a fixed-particle diameter, $d=0.7\ \mu\text{m}$, and detection angle $\theta=180^\circ$. We see that the dominant component changes from LCP to RCP as the source-detector distance increases. Figure 4 shows the backscattered time profiles for different detection angles: (a) $\cos\theta=-1$, (b) $\cos\theta=-0.9$, (c) $\cos\theta=-0.8$, for particle diameter $d=0.855\ \mu\text{m}$ and the source-detector distance $x_d=1.0l_{tr}$. While total intensity increases with a decrease of angle θ , the RCP component remains dominant, which indicates that the helicity of backscattered light is not sensitive to the angle.

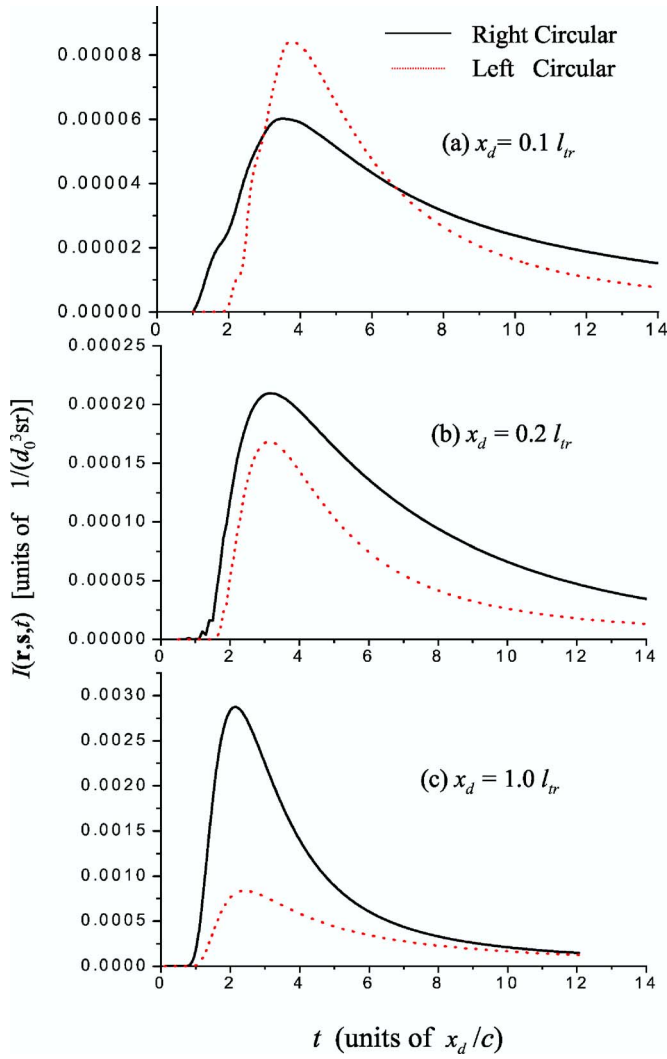


FIG. 3. (Color online) Time-resolved profiles of RCP (solid curve) and LCP (dotted curve) backscattered light as functions of time t , at different source-detector distances: (a) $x_d = 0.1 l_{tr}$, (b) $x_d = 0.2 l_{tr}$, (c) $x_d = 1.0 l_{tr}$, for particle diameter $d = 0.7 \mu\text{m}$, the detection angle $\theta = 180^\circ$, and the wavelength $\lambda = 610 \text{ nm}$. The incident beam is RCP.

B. Comparison with experiments

We compare the above theoretical result with that of our experiments [23]. The setup for the time-resolved backscattering experiment is schematically shown in Fig. 5. The sample comprises polystyrene spheres suspended in deionized water in a $6 \times 6 \times 10 \text{ cm}^3$ glass cell. Ultrashort light pulses of 100 fs duration are generated at a repetition rate of 82 MHz with wavelength $\lambda = 610 \text{ nm}$ by a colliding pulse mode-locked dye laser. A quarter-wave plate is used to obtain RCP light. Time-resolved circularly polarized backscattered light is monitored by a 2 ps resolution streak camera.

Figure 6 shows the time-resolved profiles of backscattered light measured separately, with (a) small particles $d = 0.213 \mu\text{m}$ ($g = 0.389$), scattering coefficients $\mu_s/c = 0.61 \text{ cm}^{-1}$ ($l_{tr} = 2.68 \text{ cm}$), and (b) large particles $d = 8.0 \mu\text{m}$ ($g = 0.911$), scattering coefficients

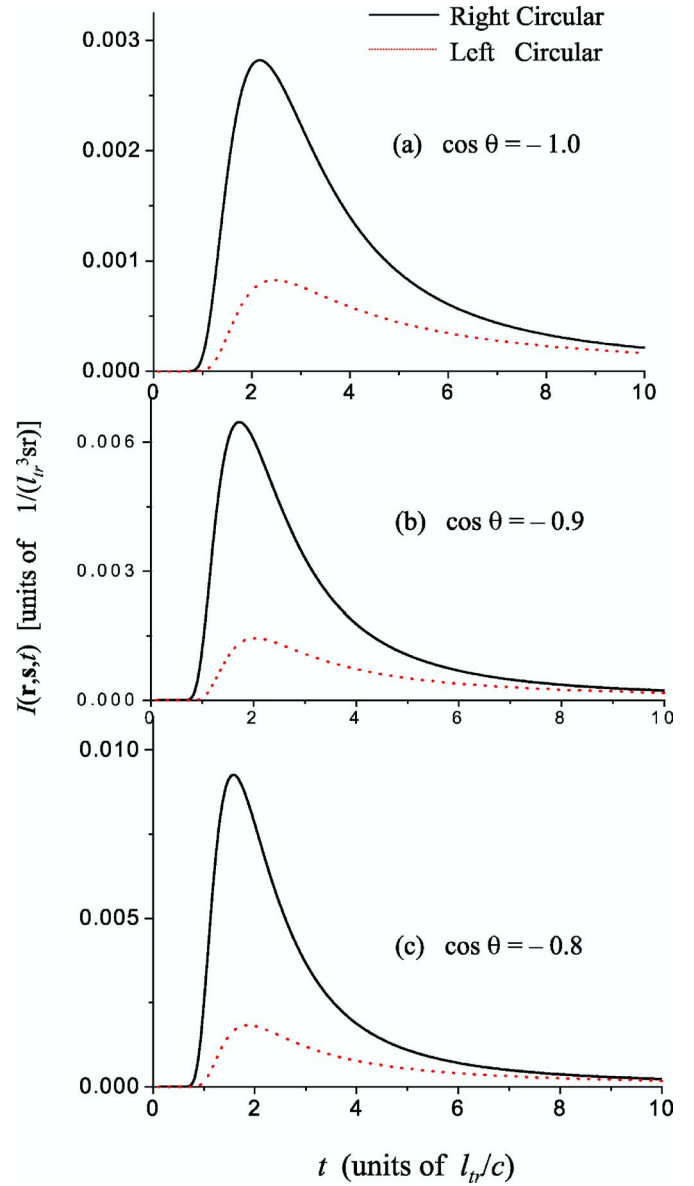


FIG. 4. (Color online) Time-resolved profiles of RCP (solid curve) and LCP (dotted curve) backscattered light as functions of time t , at different angles: (a) $\cos \theta = -1$, (b) $\cos \theta = -0.9$, (c) $\cos \theta = -0.8$, for the particle's diameter $d = 0.855 \mu\text{m}$, the detector position $x_d = 1.0 l_{tr}$, and the wavelength $\lambda = 610 \text{ nm}$. The incident beam is RCP.

$\mu_s/c = 0.61 \text{ cm}^{-1}$ ($l_{tr} = 18.42 \text{ cm}$). The detected backscattered light is dominated by the LCP (dotted curve) for small particles in case (a), but it is dominated by the RCP (solid curve) for large particles in case (b), even though the average x_d/l_{tr} for case (b) is much smaller than that for case (a). Figure 7 shows a comparison of normalized circularly polarized intensity of theoretical and experimental results for the case of $d = 8.0 \mu\text{m}$ ($d/\lambda = 13.11$). Considering the differences between the theoretical parameters and the experimental setup (not an infinite medium, uncertainty in source-detector distance) theoretical predictions are in reasonable agreement with the experimental result.

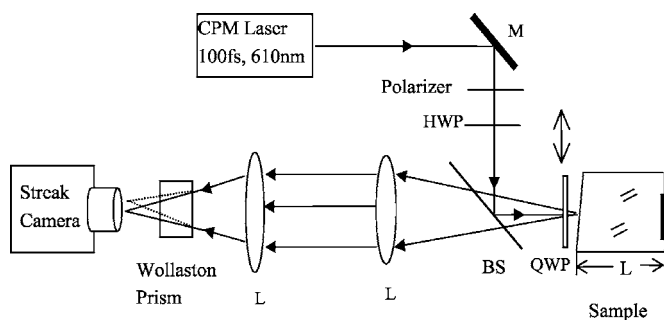


FIG. 5. Schematic diagram of the experimental setup for the time-resolved polarized backscattering measurement (BS=beam splitter, L=lens, M=mirror).

IV. DISCUSSION

A detailed theoretical formalism for the calculation of the distribution of polarized light intensity scattered from an infinite uniform turbid medium has been presented. The formalism is based on an analytical cumulant solution of the vector radiative transfer equation for an arbitrary phase matrix. It is then specialized for a phase matrix obtained from the Mie theory since many practical applications deal with Mie-scattering cases. The scattered polarized photon distri-

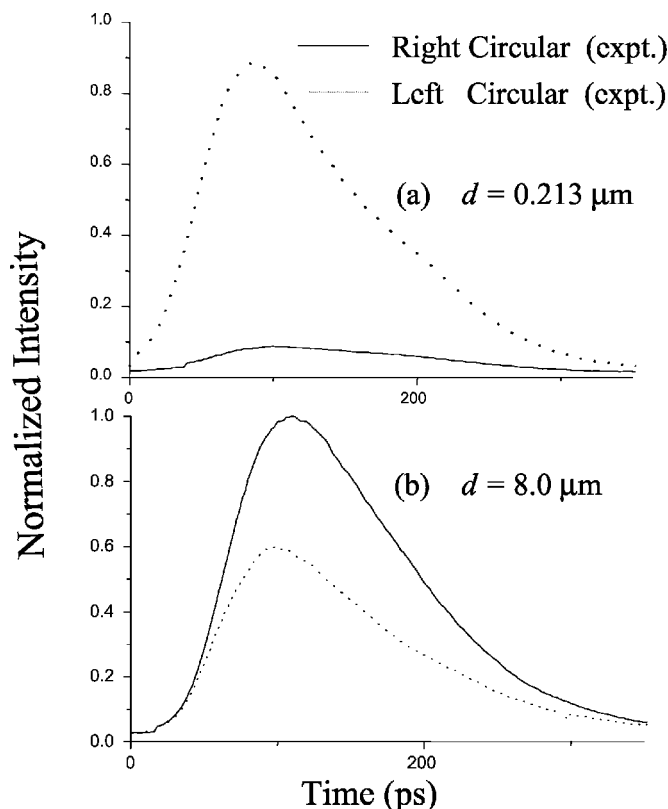


FIG. 6. The experimental time-resolved profiles of RCP (solid curve) and LCP (dotted curve) backscattered light as functions of time t for (a) small particles $d=0.213 \mu\text{m}$ ($g=0.389$), the scattering coefficients $\mu_s/c=0.61 \text{ cm}^{-1}$ ($l_{tr}=2.68 \text{ cm}$), (b) large particles $d=8.0 \mu\text{m}$ ($g=0.911$), $\mu_s/c=0.61 \text{ cm}^{-1}$ ($l_{tr}=18.42 \text{ cm}$). The incident beam is RCP.

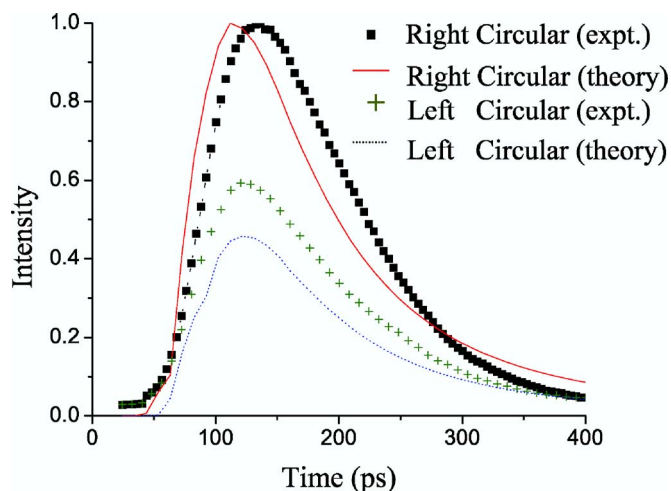


FIG. 7. (Color online) Comparison of theoretical and experimental results of normalized circular polarized light intensity for the medium with a particle diameter $d=8.0 \mu\text{m}$ and wavelength $\lambda=610 \text{ nm}$. The incident beam is RCP.

bution depends on the size of the scatterers, the distance between the light source and the detector, as well as, on the detection angle.

The advantage of the analytical cumulant solution is that it enables the fast and accurate calculation of the temporal profile of scattered polarized photon distribution. The use of Stoke's representation allows the investigation of light of any polarization state, including linear polarization and circular polarization, which are commonly used in practical applications. We have used a collimated ultrashort input pulse in our formalism, which represents the experimental conditions using picosecond and femtosecond lasers more closely than the plane wave cases used by earlier works [1–6,8,9]. In our formalism, the linear polarization case is handled by setting the initial Stokes vector as $[1, 1, 0, 0]$. Our initial results for linear polarization are in good agreement with earlier results [4,5].

In this paper, the focus has been on the calculation of circularly polarized light intensity in the backscattering geometry. The formalism enables the calculation of the intensity distribution of multiple backscattered light components that are copolarized and cross polarized with the incident beam for different angles of detection and for different source-detector positions. It is applicable for the analysis of three-dimensional spatially resolved measurements of characteristics of scattering media, such as satellite-based lidar measurements of clouds and aerosols. The approaches using a plane-wave incident beam calculate the backscattered photon flux at the plane of incidence ($z=0$ plane), and simplify the three-dimensional probing problem as a one-dimensional problem [2–6,8,9]. The approaches using Monte Carlo simulation can also handle three-dimensional spatially resolved measurements, but require a long computation time [7,39,40].

Once the copolarized and cross-polarized scattered intensity distributions are calculated, parameters, such as the degree of polarization and image contrast can be readily calculated to take advantage of the polarization memory effect

[25]. One of the results of this work elucidates the dependence of the relative intensities of the backscattered copolarized and cross-polarized light on the size of the scatterers in the turbid medium. We find that when the incident light is right circularly polarized, the backscattered signal is dominated by LCP light if the size of scatterers is smaller than the wavelength of light, but it is dominated by RCP light if the scatterer size is larger than the wavelength of light. The conclusion is in good agreement with our experimental results [23]. The dependence of the helicity of circularly polarized backscattered light on the scatterer size, and the polarization memory effect have been investigated by other authors [6,9,25–27,41]. Mackintosh *et al.* [25] experimentally demonstrated the polarization memory effect for spherical particles suspended and undergoing Brownian motion in a liquid by fitting a simple diffusion-based model to account for temporal correlations of the intensity fluctuations for different polarization channels. The theoretical estimation of backscattering of the circular polarized light using the numerical solution of the VRTE has been performed by Kim and Moscoso [6], as well as Sakami and Dogariu [9], which has been mentioned earlier in the Introduction. Phillips *et al.* [41] used an electric-field Monte Carlo method to study the backscattering of circularly polarized beams normally incident on a half space of scattering particles and found that the backscattered light of the same helicity formed a ring centered on the point of incidence. A Monte Carlo approach has been used by other researchers as well [7,39,40]. Xu and Alfano [27] used a random-walk approach to analytically estimate the characteristic depolarization length, which is obtained as an average over the entire detection solid angle. All these approaches converge on the general result that the circularly polarized light of the same helicity dominates backscattering when the scatterer size is larger than the light wavelength, as does the formalism presented in this paper and experimental results [23]. The salient feature of this work is that it provides an analytical approach for the calculation of polarized scattered light intensity, an experimentally measurable quantity, as a function of time, detection angle, and source-detector separation.

The dependence of the polarized backscattered light on the size of the scatterers in the medium has many potential applications, including biomedical imaging [13–15], flow cytometry [18,19], investigation of biological cell differentiation [17,18], subsurface imaging of cracks and corrosion below paint layers [42,43], lidar-based remote sensing of investigation of cloud and aerosol distribution in atmosphere [20,21], and the imaging of targets in turbid water [22].

Biomedical and biophysical applications represent an increasingly important area of application of polarized light scattering. As early as 1976, polarized light scattering was identified as a “new biophysical tool” [6]. The scatterers in biological materials include cells, cell nuclei, mitochondria that are in the Mie scattering domain (typical size varies from 5–20 μm as compared to the wavelength of light in the visible to NIR of 0.5–1.5 μm). Polarization effects in scattered light have been used to study bacterial suspensions in water [16,19], distinguish between a number of leukocyte types in flow cytometry [44,18], cell differentiation [17], and polynucleosome superstructures [45]. It has recently been

shown experimentally that backscattered light may be analyzed to obtain information about the size distribution of the cell nuclei [15,46], which in turn could be useful for cancer detection as the cell nucleus size, shape, and distribution changes with cancer progression. In biomedical imaging applications polarization effects in scattering have been shown to be useful in examining skin [47], and subsurface structures in the prostate and other tissues [48].

Another important area of application of polarized light scattering is the remote sensing of the atmosphere and earth. Radar technology, the workhorse for remote sensing of the earth and the atmosphere, makes use of radio waves and its depolarization to obtain information about remote targets and ground flora [49]. While single-scattering approximation of radio waves is reasonable for radar applications [1], for probing of dense cloud, fog, and aerosols in the atmosphere, multiple scattering of light needs to be considered, which the formalism developed in this article does. Different scatterers in the atmosphere have varied size distributions [1,50], such as cloud and fog droplets (radii generally $<100 \mu\text{m}$, mean radii typically 2.5–5 μm), aerosols (typically $<1 \mu\text{m}$), and hydrometeors (typically 1 μm or higher). Lidar-based investigation of cloud, aerosols, and other atmospheric scatterers employ visible and near-infrared light (typically 532 nm and 1064 nm) [20,51]. Scatterer size to wavelength ratio dictates the use of Mie theory for the study of light scattering by clouds and aerosols. In the CALIPSO (Cloud-Aerosol Lidar and Infrared Pathfinder Satellite Observations) mission of NASA [51] one of the tasks involves probing with linearly polarized 532 nm and 1064 nm nanosecond duration pulses and the analysis of the temporal profiles of backscattered light for assessing the vertical distribution of clouds and aerosols in the atmosphere. Pal and Carswell [21] have observed spatial variations in the polarization properties of multiple-scattered light backscattered from clouds. Clearly these types of experimental data and those obtained by extending measurements to even shorter pulses and circularly polarized beams are fertile grounds for the application of the formalism presented in this paper.

ACKNOWLEDGMENTS

This work was supported in part by NASA URC—Center for Optical Sensing and Imaging at CCNY (NASA Grant No. NCC-1-03009), by the Office of Naval Research (ONR), and in part by U.S. Army Medical Research and Materials Command.

APPENDIX: CLEBSCH-GORDAN COEFFICIENTS AND d -FUNCTION

For the convenience of the reader, we list the formula of angular momentum we used in this paper.

The following formula for Clebsch-Gordan coefficients $\langle l-h, 1, m, -j | l, m-j \rangle$ are useful for our calculation,

$$\langle l-h, 1, m, -j | l, m, -j \rangle = \begin{Bmatrix} \left[\frac{(l-m)(l-m+1)}{2l(2l-1)} \right]^{1/2} & \left[\frac{(l+m)(l-m+1)}{2l(l+1)} \right]^{1/2} & \left[\frac{(l+m)(l+m+1)}{(2l+2)(2l+3)} \right]^{1/2} \\ \left[\frac{(l-m)(l+m)}{l(2l-1)} \right]^{1/2} & \frac{m}{[l(l+1)]^{1/2}} & - \left[\frac{(l+m+1)(l-m+1)}{(l+1)(2l+3)} \right]^{1/2} \\ \left[\frac{(l+m)(l+m+1)}{2l(2l-1)} \right]^{1/2} & - \left[\frac{(l-m)(l+m+1)}{2l(l+1)} \right]^{1/2} & \left[\frac{(l-m)(l-m+1)}{(2l+2)(2l+3)} \right]^{1/2} \end{Bmatrix}, \quad (30)$$

where the row index (from above) $j=1, 0, -1$ and the column index (from left) $h=1, 0, -1$.

For obtaining $d_{mn}^l(x)$, the following recurrence relation is used:

$$\begin{aligned} d_{mn}^l(x) = & \frac{1}{(l-1)[(l^2-m^2)(l^2-n^2)]^{1/2}} \\ & \times \{(2l-1)[l(l-1)x-mn]d_{mn}^{l-1}(x) \\ & - l[(l-1)^2-m^2][(l-1)^2-n^2]^{1/2}d_{mn}^{l-2}(x)\}, \end{aligned} \quad (31)$$

for $l > \max(|m|, |n|)$, with

$$\begin{aligned} d_{mn}^{\max(|m|, |n|)}(x) = & \frac{1}{2^{\max(|m|, |n|)} [(m-n)!(m+n)!]^{1/2}} \\ & \times (1-x)^{|m-n|/2} (1+x)^{|m+n|/2}, \end{aligned} \quad (32)$$

and $d_{mn}^l(x)=0$ for $l < \max(|m|, |n|)$. For $m=0, n=0$ we have $d_{00}^0(x)=1$, $d_{00}^1(x)=x$, and

$$ld_{00}^l(x) = (2l-1)xd_{00}^{l-1}(x) - (l-1)d_{00}^{l-2}(x). \quad (33)$$

-
- [1] A. Ishimaru, *Wave Propagation and Scattering in Random Media* (Institute of Electrical and Electronic Engineers, New York, 1997).
- [2] R. L. T. Cheung and A. Ishimaru, *Appl. Opt.* **21**, 3792 (1982).
- [3] Q. Ma, A. Ishimaru, and Y. Kuga, *Radio Sci.* **25**, 419 (1990).
- [4] A. Ishimaru, S. Jaruwatanadilok, and Y. Kuga, *Appl. Opt.* **40**, 5495 (2001).
- [5] A. D. Kim and M. Moscoso, *Phys. Rev. E* **64**, 026612 (2001); *SIAM J. Comput.* **23**, 2075 (2002).
- [6] A. D. Kim and M. Moscoso, *Opt. Lett.* **27**, 1589 (2002).
- [7] R. Vaillon, B. T. Wong, and M. P. Mengüç, *J. Quant. Spectrosc. Radiat. Transf.* **84**, 383 (2004).
- [8] Y. Jiang, Y. L. Yung, S. P. Sander, and L. D. Travis, *J. Quant. Spectrosc. Radiat. Transf.* **84**, 169 (2004).
- [9] M. Sakami and A. Dogariu, *J. Opt. Soc. Am. A* **23**, 664 (2006).
- [10] A. A. Kokhanovsky, *Light Scattering Media Optics: Problems and Solutions*, 3rd ed. (Springer and Praxis Publishing, Chichester, 2004).
- [11] D. Bicout, C. Brosseau, A. S. Martinez, and J. M. Sedhmitt, *Phys. Rev. E* **49**, 1767 (1994).
- [12] R. Carminati, R. Elaloufi, and J. J. Greffet, *Phys. Rev. Lett.* **92**, 213903 (2004).
- [13] A. H. Hielscher, J. R. Mourant, and I. Bigio, *Appl. Opt.* **36**, 125 (1997).
- [14] S. G. Demos and R. R. Alfano, *Appl. Opt.* **36**, 150 (1997).
- [15] V. Backman, R. Gurjar, K. Badizadegan, I. Itzkan, R. R. Dasari, L. T. Perelman, and M. S. Feld, *IEEE J. Sel. Top. Quantum Electron.* **5**, 1019 (1999).
- [16] W. S. Bickel, J. F. Davidson, D. R. Huffman, and R. Kilkson, *Proc. Natl. Acad. Sci. U.S.A.* **73**, 486 (1976).
- [17] W. S. Bickel and M. E. Stafford, *J. Biol. Phys.* **9**, 53 (1981).
- [18] B. G. deGroot, L. W. M. M. Terstappen, G. J. Puppels, and J. Greve, *Cytometry* **8**, 539 (1987).
- [19] B. V. Bronk, W. P. van de Merwe, and M. Stanley, *Cytometry* **13**, 155 (1992).
- [20] D. M. Winker, W. H. Hunt, and C. A. Hostetler, *Proceedings of Laser Radar Techniques for Atmospheric Sensing*, edited by U. N. Singh [Proceedings of SPIE **5575**, 8 (2004)].
- [21] S. R. Pal and A. I. Carswell, *Appl. Opt.* **24**, 3464 (1985).
- [22] G. W. Kattawar and M. J. Rakovic, *Appl. Opt.* **38**, 6431 (1999).
- [23] X. Ni and R. R. Alfano, *Opt. Lett.* **29**, 2773 (2004).
- [24] G. D. Lewis, D. L. Jordan, and P. J. Roberts, *Appl. Opt.* **38**, 3937 (1999).
- [25] F. C. MacKintosh, J. X. Zhu, D. J. Pine, and D. A. Weitz, *Phys. Rev. B* **40**, 9342 (1989).
- [26] F. C. MacKintosh and S. John, *Phys. Rev. B* **40**, 2383 (1989).
- [27] M. Xu and R. R. Alfano, *Phys. Rev. Lett.* **95**, 213901 (2005); *Phys. Rev. E* **72**, 065601 (2005).
- [28] W. Cai, M. Lax, and R. R. Alfano, *Phys. Rev. E* **61**, 3871 (2000).
- [29] W. Cai, M. Lax, and R. R. Alfano, *J. Phys. Chem. B* **104**, 3996 (2000).
- [30] W. Cai, M. Xu, and R. R. Alfano, *Phys. Rev. E* **71**, 041202 (2005).
- [31] W. Cai, M. Lax, and R. R. Alfano, *Phys. Rev. E* **63**, 016606 (2000).
- [32] M. Born and E. Wolf, *Principles of Optics*, 7th ed. (Cambridge University Press, Cambridge, England, 2002).

- [33] S. Chandrasekhar, *Radiative Transfer* (Clarendon, Oxford, 1950).
- [34] I. Kuščer and M. Ribarič, *Opt. Acta* **6**, 42 (1959).
- [35] J. W. Hovenier and C. V. M. van der Mee, *Astron. Astrophys.* **128**, 1 (1983).
- [36] B. M. Brink and G. M. Satchler, *Angular Momentum* (Clarendon Press, Oxford, 1962).
- [37] M. I. Mishchenko, L. D. Travis, and A. A. Lacis, *Scattering, Absorption, and Emission of Light by Small Particles* (Cambridge University Press, Cambridge, 2002).
- [38] R. P. Feynman, *Phys. Rev.* **84**, 108 (1951).
- [39] M. J. Rakovic, G. W. Kattawar, M. Mehrubeoglu, B. D. Cameron, L. V. Wang, S. Rastegar, and G. L. Cote, *Appl. Opt.* **38**, 3399 (1999).
- [40] S. Bartel and A. H. Hielscher, *Appl. Opt.* **39**, 1580 (2000).
- [41] K. G. Phillips, M. Xu, S. K. Gayen, and R. R. Alfano, *Opt. Express* **13**, 7954 (2005).
- [42] J. H. Ali, W. B. Wang, P. P. Ho, and R. R. Alfano, *Opt. Lett.* **25**, 1303 (2000).
- [43] J. H. Ali, W. B. Wang, R. R. Alfano, and M. K. Kassir, *Theor. Appl. Fract. Mech.* **41**, 1 (2000).
- [44] G. C. Salzman, S. B. Singham, R. G. Johnston, and C. F. Bohren, in *Flow Cytometry and Sorting*, 2nd ed. (Wiley-Liss, New York, 1990).
- [45] S. Zeitz, A. Belmont, and Nicolini, *Cell Biophys.* **5**, 163 (1983).
- [46] L. T. Perelman, V. Backman, M. Wallace, G. Zonnois, R. Manoharan, A. Nusrat, S. Shields, M. Seiler, T. Hamano, I. Itzkan, J. van Dam, J. M. Crawford, and M. S. Feld, *Phys. Rev. Lett.* **80**, 627 (1998).
- [47] R. R. Anderson, *Arch. Dermatol.* **127**, 1000 (1991).
- [48] W. B. Wang, J. H. Ali, R. R. Alfano, J. H. Vitenson, and J. M. Lombardo, *IEEE J. Sel. Top. Quantum Electron.* **9**, 228 (2003).
- [49] M. I. Skolnik, *Introduction to Radar Systems* (McGraw-Hill, New York, 1962).
- [50] V. E. Zuev, A. A. Zemlyanov, Y. D. Kopytin, and A. V. Kuzikovskii, *High-Power Laser Radiation in Atmospheric Aerosols* (D. Reidel Publishing, Dordrecht, 1984).
- [51] D. M. Winker, J. R. Pelon, and M. P. McCormick, *Proceedings of the Conference of Lidar Remote Sensing for Industry and Environment Monitoring III*, edited by U. N. Singh, T. Itabe, and Z. Liu [Proceedings of SPIE **4893**, 1 (2003)].

Determination of light absorption, scattering and anisotropy factor of a highly scattering medium using backscattered circularly polarized light

M. Xu^a, M. Alrubaiee^b, S. K. Gayen^b and R. R. Alfano^b

^aDepartment of Physics, Fairfield University, Connecticut, CT 06824

^bInstitute for Ultrafast Spectroscopy and Lasers and Department of Physics,
The City College and Graduate Center of City University of New York, New York, NY 10031
Email: mxu@mail.fairfield.edu

ABSTRACT

The absorption coefficient, the scattering coefficient and the anisotropy factor of a highly scattering medium are determined using the diffuse reflectance of an obliquely incident beam of circularly polarized light. This approach determines both the anisotropy factor and the cutoff size parameter for the fractal continuous scattering medium such as biological tissue and tissue phantoms from depolarization of the backscattered light.

Keywords: absorption, scattering, anisotropy factor, backscattering, depolarization, circular polarization, tissue, turbid medium

1. INTRODUCTION

The estimation of the optical properties (absorption coefficient μ_a and scattering coefficient μ_s) and the anisotropy factor (g) of a turbid medium is an important problem in atmospheric, biomedical and hydrologic optics. Light diffuses in a highly scattering medium, whose behavior essentially depends on the reduced scattering coefficient $\mu'_s = \mu_s(1 - g)$. The diffusion of light remains almost the same when varying μ_s and g yet keeping μ'_s unchanged. This explains why μ_a and μ'_s , instead of μ_a , μ_s and g , are commonly used in optical imaging. Light absorption and scattering coefficients depend on the optical properties of constituent particles and their concentration. The g -factor measures how much forward peaked is the angular distribution of light when it is scattered once by a particle in the medium, and is independent of the concentration of the scatterers. The value of the g -factor correlates strongly with the size of the scatterer. Determination of the g -factor then provides a direct probe of the size of scatterer, which constitutes one useful fingerprint in discriminating normal and diseased tissues.^{1, 2}

One way to estimate the g -factor is to use an iterative method that consists of repeatedly solving the corresponding direct radiative transfer problem by, for example, Monte Carlo simulations, with updated optical properties until the irradiance matches the measured values.³ Explicit analytical equations have also been developed (analytic inverse radiative transfer method) for determining the optical properties in the simplest problems.⁴ In both approaches, the type of the phase function of light scattering by the medium is usually assumed known and the Henyey-Greenstein phase function⁵ has been commonly used.

In this paper, we report on a scheme of detecting light absorption coefficient, scattering coefficient and the g -factor simultaneously from measurement of the circularly polarized backscattered light at different positions along a line. Light is obliquely incident on the surface of the medium with an incidence angle ~ 70 degree. Both co-polarized and cross-polarized backscattered light are measured. The difference of the backscattered co-polarized and cross-polarized light intensities is used to find the g -factor of the medium. Experimental demonstrations of this approach to obtain the three parameters (absorption coefficient, scattering coefficient and the g -factor) of tissue phantoms are presented.

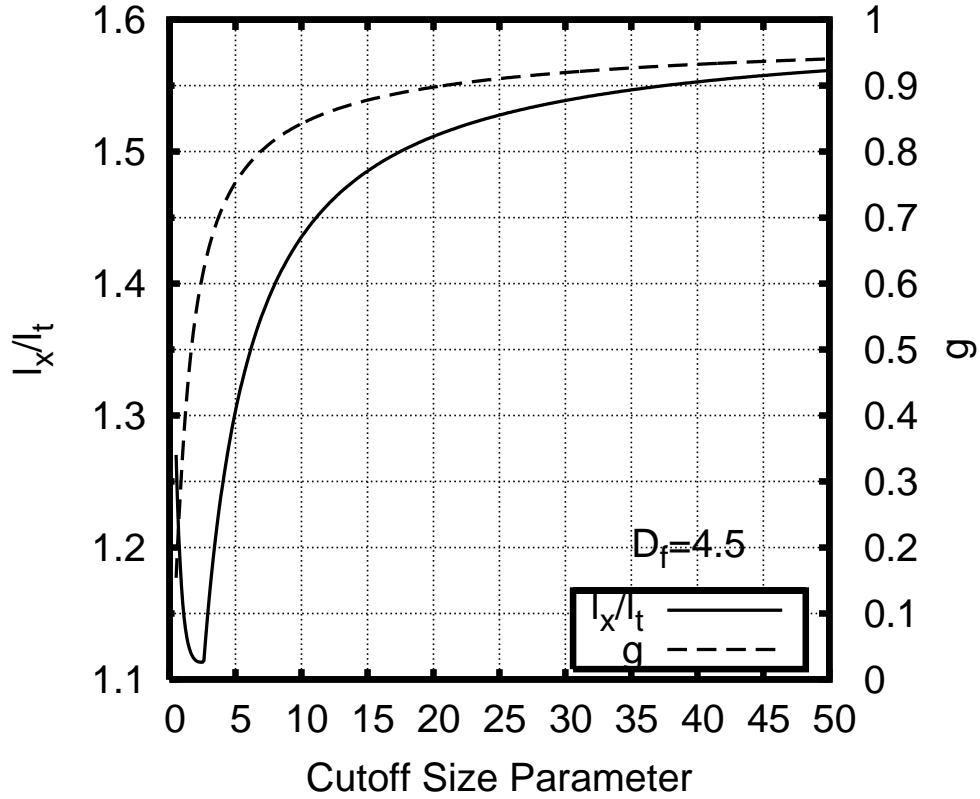


Figure 1. The ratio of the uncoiling length over the transport mean free path l_x/l_t and the anisotropy factor g of soft tissue of a fractal dimension 4.5 and of varying cutoff size parameter $X = 2\pi n l_{\max}/\lambda$.

2. THEORETICAL FORMALISM AND EXPERIMENTAL METHOD

Light propagation in a turbid medium can be described by radiative transfer theory. Diffusion approximation to radiative transfer theory is a valid model for light propagation if the medium is highly scattering and optically thick. For a polarized incident beam, light propagation in the medium accompanies its depolarization. The characteristic lengths governing light depolarization in turbid media have been obtained earlier.^{6,7} The depolarization of circularly polarized light is found to be determined by the uncoiling length l_x , the distance over which the degree of circular polarization of the beam drops by $1/e$. The uncoiling length for a turbid medium is given by⁷

$$l_x \equiv \mu_s^{-1} / \ln \frac{1}{\lambda_x} \quad (1)$$

where $\lambda_x = \max(\Lambda_0, \Lambda_1)$, $\Lambda_0 = \frac{1}{2\gamma} \int_{-1}^1 \Re[S_1^* S_2] d\mu$, $\Lambda_1 = \frac{1}{2\gamma} \int_{-1}^1 \Re[S_1^* S_2] \mu d\mu$, $\gamma = \frac{1}{4} \int_{-1}^1 (|S_1|^2 + |S_2|^2) d\mu$, $\mu \equiv \cos \theta$, and $S_{1,2}(\theta)$ is the amplitude scattering function with θ the scattering angle.⁸

Light scattering by biological tissue and cells can be described by the fractal continuous random medium model.^{1,2} In this model, tissue light scattering is determined by two morphological parameters: the fractal dimension D_f and the cutoff correlation length l_{\max} . The parameter D_f reveals the weight of small vs large scattering centers in the sample and l_{\max} measures the maximum size of scattering centers. Light depolarization characteristic lengths, including the uncoiling length l_x , in biological tissue and tissue phantoms have been investigated.⁹ Fig. (1) displays the ratio l_x/l_t and the g-factor versus the cutoff size parameter $X = 2\pi n l_{\max}/\lambda$ for a fractal continuous random medium with $D_f = 4.5$ where n is the refractive index of the medium and λ is the wavelength of the incident beam in vacuum. This figure suggests that the anisotropy factor g (and l_{\max}) can be determined if the fractal dimension D_f and the uncoiling length l_x can be found in addition to the transport mean free path l_t .

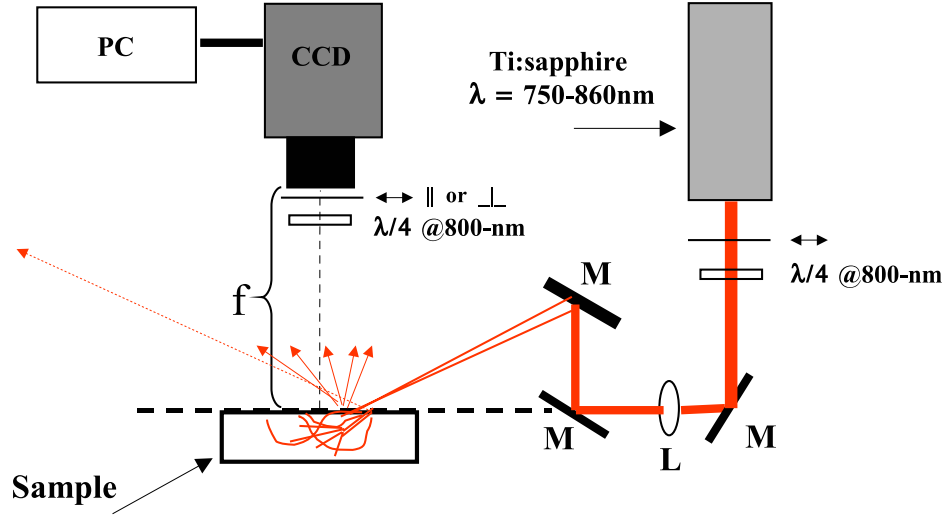


Figure 2. Schematic diagram of the experimental setup. M stands for mirror, L lens, and f is the focal length of the CCD camera. The $\lambda/4$ wave plates and polarizers are used to generate a circularly polarized beam and to detect co- or cross-polarized light at the wavelength of 800nm.

Our procedure for the determination of μ_a , μ_s and g is as follows. First μ_a and μ'_s are determined from the diffuse reflectance of the sample for an obliquely incident beam at various wavelengths centering at λ . Second, the fractal dimension D_f is determined from $\mu'_s(\lambda) \propto \lambda^{3-D_f}$. Third, the uncoiling length l_x is found from the depolarized diffuse reflectance of a circularly polarized incident beam. And finally, the anisotropy factor g is obtained by the ratio of l_x/l_t (see Fig. 1). The first two steps can be combined to retrieve μ_a , μ'_s and D_f simultaneously from fitting to the diffuse reflectance data at all wavelengths together assuming the power law for $\mu'_s(\lambda)$ is strictly satisfied.

For an obliquely incident pencil beam at the origin on the surface $z = 0$ of the sample and propagating in the direction $(\sin \alpha, 0, -\cos \alpha)$ where α is the angle of incidence, the initial ballistic motion of the beam within the medium is in the direction $(\sin \beta, 0, -\cos \beta)$ where $n \sin \beta = \sin \alpha$. The diffuse reflectance at the position $(x, y, 0)$ on the surface is given by¹⁰

$$R(x, y) = \frac{l_t \cos \beta}{4\pi \rho_1^3} (1 + \mu_{\text{eff}} \rho_1) \exp(-\mu_{\text{eff}} \rho_1) + \frac{l_t \cos \beta + 2z_e}{4\pi \rho_2^3} (1 + \mu_{\text{eff}} \rho_2) \exp(-\mu_{\text{eff}} \rho_2), \quad (2)$$

where $\mu_{\text{eff}} = \sqrt{3\mu_a/l_t}$, $\rho_1 = \sqrt{(x - l_t \sin \beta)^2 + y^2 + l_t^2 \cos^2 \beta}$, and $\rho_2 = \sqrt{(x - l_t \sin \beta)^2 + y^2 + (2z_e + l_t \cos \beta)^2}$. The parameter z_e is the extrapolation length, dependent on the refractive index mismatch at the interface.¹¹ Eq. (2) is used to fit the measured diffuse reflectance along a line in the x direction on the surface to obtain μ_a and l_t .

For an incident circularly polarized beam, light depolarization presents one extra channel that light leaves the co-polarized state to the cross-polarized state. Denote the co-polarized and cross-polarized backscattered light intensity for an incident circularly polarized light as I_{\pm} , respectively. The depolarized diffuse reflectance is proportional to $\Delta I = I_+ - I_-$ and can be modelled by the same expression (2) with the only modification of $\mu_a \rightarrow \mu'_a = \mu_a + l_x^{-1}$. The same technique hence can be used to fit for l_x in the region far away from the incidence point where the diffusion model is valid.

The experimental setup is shown in Fig. 2. The light source is a Ti:sapphire laser (Spectra-Physics Tsunami) tunable over the 750–860nm spectral range. The laser was operated in CW mode by turning off the acousto-optic modulator and had a spectral FWHM (full width at half maximum) bandwidth less than 1nm. The beam passes through a converging lens (focal length 40cm) and focused on the surface of the sample after elevated using a periscope mirror configuration. The incidence angle is set to be $\alpha = 72.4^\circ$. The refractive index of the diluted Intralipid-10% suspension is $n = 1.334$ and the extrapolation length is computed to be $z_e = 1.69l_t$.¹¹ Backscattered light in the direction normal to the surface of the sample is recorded by a CCD camera for the wavelengths from 760nm to 860nm with a step of 10nm.

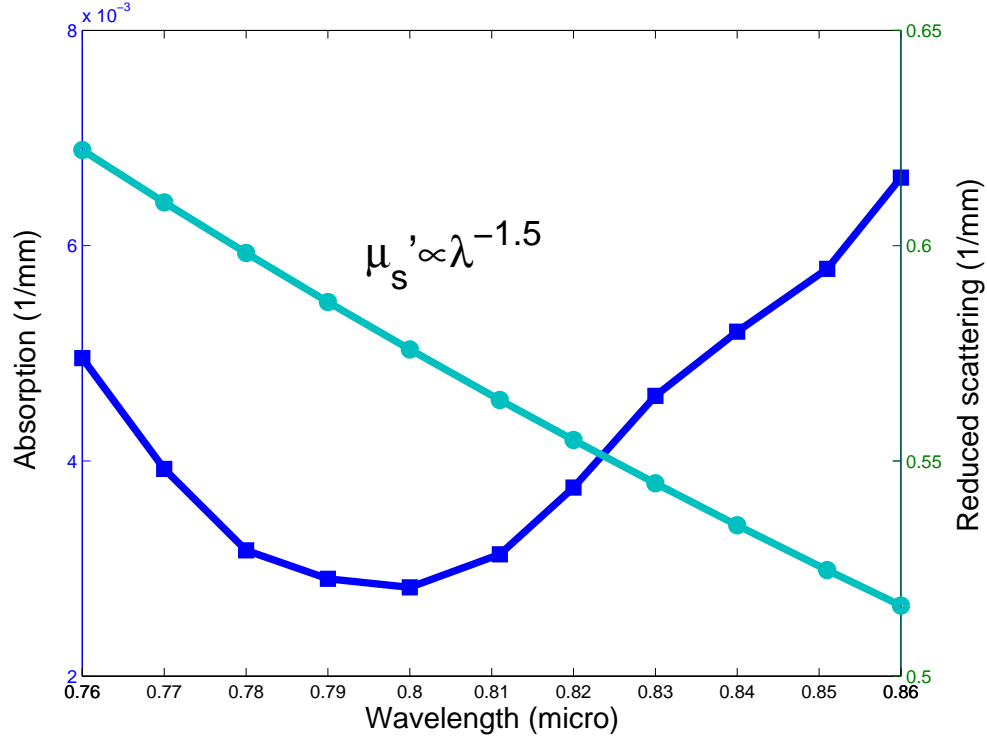


Figure 3. The wavelength dependence of the absorption and the reduced scattering coefficients of the Intralipid-10% suspension.

3. RESULT

Fig. 3 displays the wavelength dependence of μ_a and μ'_s from fitting the total diffuse reflectance where light is collected regardless of its polarization. The absorption spectrum follows essentially that of water. The wavelength dependence of the reduced scattering coefficient follows $\mu'_s \propto \lambda^{-1.5}$. The fractal dimension of the Intralipid-10% suspension is then 4.5. It should be noted this experimental value of D_f is a bit larger than the value ($D_f = 4.2$) obtained² from the Mie scattering computation based on the particle size distribution of the Intralipid-10% suspension measured by Staveren *et. al.*¹²

The depolarized diffuse reflectance is then measured at the wavelength of 800nm at which the absorption coefficient and the transport mean free path have been found to be $\mu_a = 0.003\text{mm}^{-1}$ and $l_t = 1.77\text{mm}$, respectively, from Fig. (3). Fig. 4 displays the total backscattered light $I = I_+ + I_-$ and the depolarized backscattered light $\Delta I = I_+ - I_-$. Nearby the origin, the intensity of the cross-polarized light is stronger than that of the co-polarized light and $\Delta I < 0$. In the far zone (the region far away from the origin), the intensity of the co-polarized light is stronger than that of the cross-polarized light and $\Delta I > 0$. Fitting of the depolarized diffuse reflectance $\propto \Delta I$ along a horizontal line $3l_t$ away from the incidence point inside the far zone yields the effective absorption $\mu'_a = 0.47\text{mm}^{-1}$. The uncoiling length is then 2.13mm and the ratio $l_x/l_t = 1.20$.

From the analysis of the depolarization property of the fractal continuous medium of $D_f = 4.5$ (see Fig. 1), both the g-factor and the cut-off size parameter are now obtained. We find $g = 0.68$ at the cutoff size parameter 3.4 with $l_{\max} = 0.32\mu\text{m}$. The values of the g-factor and the cutoff size of scatterers were reported to be 0.64 at 800nm and $0.34\mu\text{m}$ in Staveren *et. al.*¹² Their agreement demonstrates the effectiveness of our proposed method.

4. DISCUSSION AND CONCLUSION

For a range of values of l_x/l_t in Fig. 1, there may be two sets of the g-factor and the cutoff size parameter giving the same ratio l_x/l_t . It does not pose any difficulty. The left branch of the l_x/l_t curve when the cutoff size parameter curve is less than 2.6 corresponds to $I_+ < I_-$ and its right branch corresponds to $I_+ > I_-$ far away from the incidence point.⁷ The

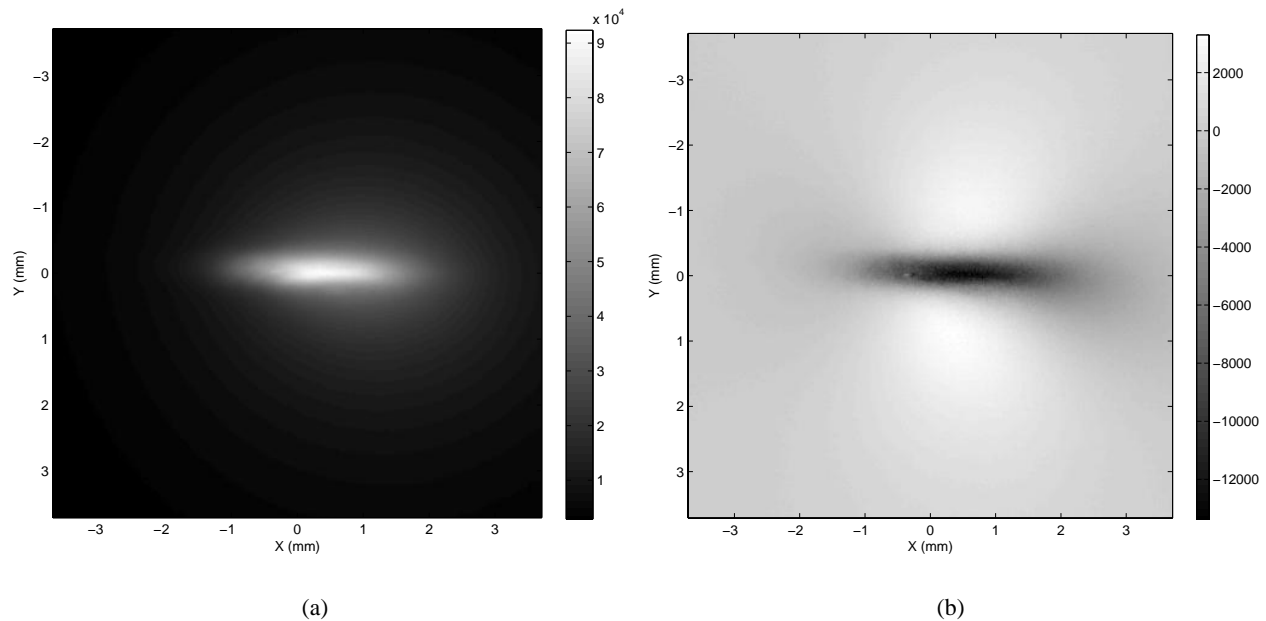


Figure 4. The intensities of backscattered light (a) the total intensity $I_+ + I_-$ and (b) the depolarized intensity $I_+ - I_-$. The circularly polarized light is incident on the origin and with an incident angle of 72.4° . The CCD camera measures I_\pm directly.

experiment shows that $I_+ > I_-$ in the far zone (see Fig. 4b) and the right branch of the l_x/l_t curve should be used in our data analysis.

The absorption coefficient, the scattering coefficient and the anisotropy factor of a highly scattering medium are determined using the diffuse reflectance of an obliquely incident circularly polarized light. This approach obtains simply both the anisotropy factor and the cutoff size parameter for the fractal continuous scattering medium from circular depolarization of the backscattered light.

ACKNOWLEDGMENTS

This work is supported in part by ONR, NASA and USAMRMC grants. MX acknowledges Fairfield University for start-up funds.

REFERENCES

1. M. Xu and R. R. Alfano, "Fractal mechanisms of light scattering in biological tissue and cells," *Opt. Lett.* **30**, pp. 3051–3053, 2005.
2. M. Xu, M. Alrubaiee, and R. R. Alfano, "Fractal mechanism of light scattering for tissue optical biopsy," in *Optical Biopsy VI, Proceedings of SPIE* **6091**, 2006.
3. N. Joshi, C. Donner, and H. W. Jensen, "Noninvasive measurement of scattering anisotropy in turbid materials by nonnormal incident illumination," *Opt. Lett.* **31**, pp. 936–938, 2006.
4. N. J. McCormick, "Analytic inverse radiative transfer equations for atmospheric and hydrologic optics," *J. Opt. Soc. Am. A* **21**, pp. 1009–1017, June 2004.
5. L. G. Henyey and J. L. Greenstein, "Diffuse radiation in the galaxy," *Astrophys. J.* **93**, pp. 70–83, 1941.
6. M. Xu and R. R. Alfano, "Random walk of polarized light in turbid media," *Phys. Rev. Lett.* **95**, p. 213905, 2005.
7. M. Xu and R. R. Alfano, "Circular polarization memory of light," *Phys. Rev. E* **72**, p. 065601(R), 2005.
8. H. C. van de Hulst, *Light Scattering by Small Particles*, Dover, New York, 1981.
9. M. Xu and R. R. Alfano, "Light depolarization by tissue and phantoms," in *Optical Interactions with Tissue and Cells XVII, Proceedings of SPIE* **6084**, 2006.

10. G. Marquez and L. V. Wang, "White light oblique incidence reflectometer for measuring absorption and reduced scattering spectra of tissue-like turbid media," *Opt. Express* **1**, pp. 454–460, 1997.
11. J. X. Zhu, D. J. Pine, and D. A. Weitz, "Internal reflection of diffusive light in random media," *Phys. Rev. A* **44**, pp. 3948–3959, 1991.
12. H. J. van Staveren, C. J. M. Moes, J. van Marle, S. A. Prahl, and M. J. C. van GemertJ, "Light scattering in Intralipid-10% in the wavelength range of 400-1100nm," *Appl. Opt.* **30**(31), pp. 4507–4514, 1991.